Manipulating Electric and Magnetic Light-matter interactions at the nanoscale

Mathieu Mivelle

Manipulating Electric and Magnetic Light-matter interactions at the nanoscale

Mathieu Mivelle
Chargé de Recherche CNRS
Institut des NanoSciences de Paris
Sorbonne Université

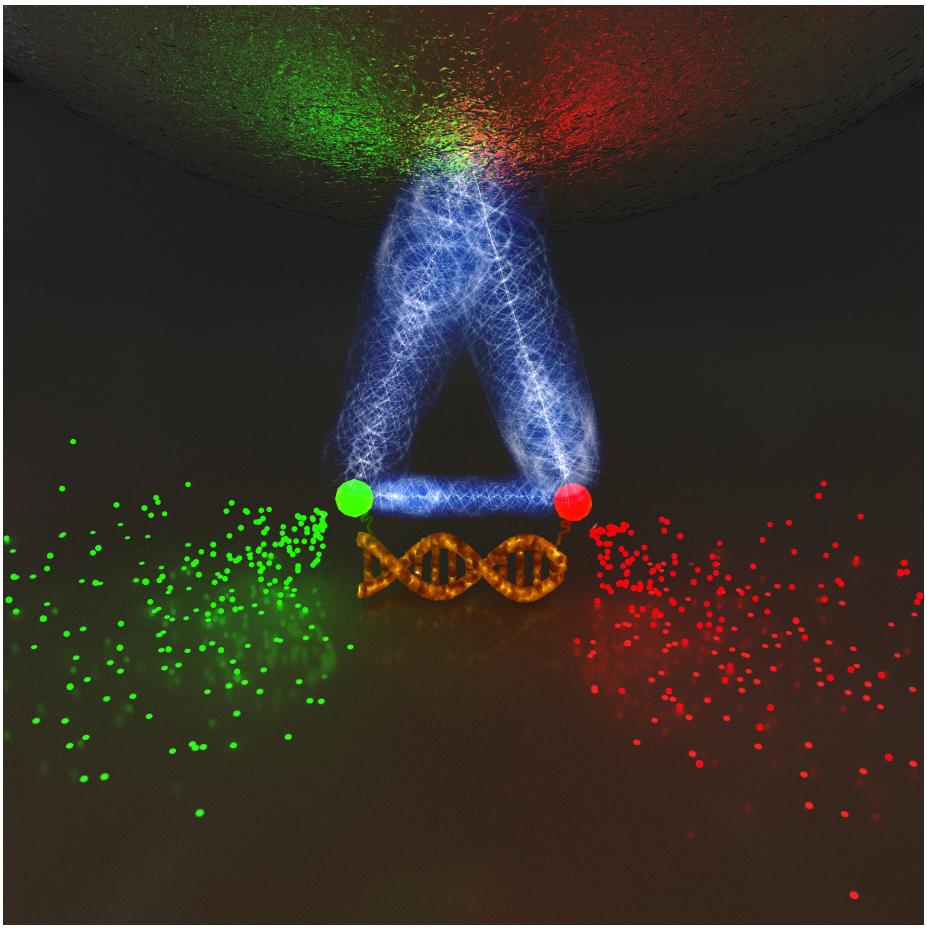

Soutenue le 27 mai 2021
Devant le jury composé de :

M. Sébastien Bidault - examinateur
M. Alexandre Bouhelier - rapporteur
Mme. Céline Fiorini-Debuisschert - rapporteure
M. Jérôme Plain - rapporteur
M. Gilles Tessier - examinateur

Table of Content

General introduction

The interactions between light and matter are present absolutely everywhere around us, and since Maxwell's work, we understand them in a much clearer way. However, we are always discovering new facets of these interactions. In particular, since the revolution in nanofabrication techniques and ever-increasing computing capabilities, we are now able to design and fabricate objects of nanometric dimensions with totally new optical properties that are not possible with macroscopic materials. This revolution has led to new scientific and technological applications, the firsts of which have been developed in our laboratories only a few years ago. For example, we can cite applications in the medical field, to kill cancer cells, in photovoltaics, to create more efficient solar panels, in cosmetics, for specific properties of sun creams, in our screens, to obtain higher quality images and colors, or in space to create ultra-reflective solar sails, etc. Of course, we are still far from controlling humans with nanorobots using the 5G network, but the advances are still significant.

Nanophotonics is remarkable in that it is now used in many fields of research. Something that was probably not foreseen at the beginning of near-field optics, the precursor field of nanophotonics. We can mention quantum information, certain parts of chemistry and biology, certain computer components, etc.

In this manuscript, I will describe, through a few chapters, the most significant researches that have shaped my research career until today. In particular, I will detail a few selected studies that illustrate my main work themes, notably my work on the manipulation and increase of electric and magnetic optical fields and their coupling to matter.

In the first part, I will describe how nanostructuring matter at nanometric scales can manipulate the electric and magnetic fields of light. In particular, by choosing suitable materials and shapes, I will explain how increasing these fields by several orders of magnitude is achievable. In the second part, I will describe examples of manipulating electric quantum emitters' emission via optical nano-antennas designed to control and concentrate the optical electric field. Finally, in the last part, I will explain how photonic nano-antennas engineered to exalt the optical magnetic field also allows manipulating quantum emitters' emission, this time, magnetic ones.

Part 1. Detecting, Manipulating and Enhancing the Electric and Magnetic fields of light

In this part, we will see through three chapters how photonic nanostructures, also called nano-antennas, can increase electric or magnetic optical fields by several orders of magnitude. In particular, in the first chapter, we will see that the design and fabrication of a bowtie aperture type antenna in a thin layer of aluminum allow, via a capacitive effect, to create an electric hot spot of a few tens of nanometers. Moreover, by placing this antenna at the end of the near-field tip, we will see that its electrical properties allow it to be used as a nanocollector and nanopolarizer of the electric-optical near-field. This first chapter is, in a way, the foundation of my scientific career since it describes the main results of my thesis, carried out at the femto-st institute of Besançon, under the direction of Fadi Baida and the co-supervision of Thierry Grosjean. This research was part of an ANR project whose goal was to characterize vectorially the electric light in the near field. Part of this chapter was also done at the IBM research center in Almaden, California, with Geoffrey Burr, where I spent several months using a Bluegene supercomputer for the simulation needs of this project.
In a second chapter, we will see that based on Babinet's principle, we can also create a plasmonic nano-antenna able to increase the optical magnetic field by several orders of magnitude, thanks in particular to the generation of intense electric currents in the skin depth of the metal. The research for this second chapter was also done during my thesis at the Femto-st institute, but it was more of a side project of the latter. The original idea for this study was suggested by Ulrich Ficher, a senior researcher at the University of Munster, who first saw the potential of the Babinet principle in the design of magnetic nanoantennas.
Finally, in a third chapter, I will describe how it is possible to design photonic nano-antennas thanks to an evolutionary algorithm to obtain nanostructures with properties superior to the antennas commonly used in nanophotonics. This third chapter comes later chronologically since the work was done after my recruitment by the CNRS and in collaboration with Sebastien Bidault and Nicolas Bonod. It is inspired by Bert Hecht's work on the design of electrical nanoantennas using a genetic algorithm. Based on this study, I have developed numerical codes to define the geometry of a photonic nanostructure that optimally meets a need. This algorithmic approach, in this period of computing expansion, will be the core of the research I want to develop in the coming years. Beyond the purely evolutionary approach, I aim to use all types of numerical optimizations proposed nowadays for the design of nanostructures but also for the realization of scientific experiments involving high repetition rate lasers, for example.

Chapter 1

An optical nano-antenna as nanosensor and nanopolarizer of electric light

The improvement of nanoscale fabrication technologies has allowed the investigation of enhanced optical phenomena on metallic and dielectric nanoparticles, leading to novel nano-antenna concepts[1], such as the multipolar[2], dipole[3,4], bowtie[5] and monopole[6] nano-antennas as well as bowtie nano-apertures[7], single particles[8] and dimers[9]. Nano-antennas are now widely used to optically interconnect free-space propagating waves together with highly localized fields for applications in the enhancement and control of the fluorescence of single emitters[10], optical tweezing[11], nanoheating[12], or non-linear optics[13,14], to name a few.

Despite many potential applications, the development of resonant nano-antennas as an optical interface between near-fields and diffraction-limited fiber modes was only recently explored at the time of my PhD. For instance, we can cite the work of Taminiau *et al* where a monopole nano-antenna has been grafted at the apex of a conventional fiber Near-field Scanning Optical Microscope (NSOM) aperture tip to probe and control single fluorescent molecules[15]. The low throughput of the aperture tip, which held the nano-antenna[16] was however a limiting factor of that system.

In this chapter, I will describe the use of a single bowtie nano-aperture (BNA) to interface diffraction-limited single-mode optical fibers with near-fields and nano-optical structures[7,17]. To improve the nano-antenna-to-fiber optical coupling, the BNA has been fabricated at the apex of a specially designed metal-coated tapered tip. And as a first application, we use this fiber probe as an integrated nanocollector for NSOM since it behaves as a high resolution polarizing nanocollector with little sensitivity to the magnetic optical field. In particular, we'll see that this system allows us to retrieve vectorial information of the electric near-field of a photonic crystal cavity.

1.1. A near-field detector of vectorial electric-light

The design of our nano-antenna fiber probe, shown schematically in Figure 1.1, consists of a single bowtie nano-aperture (BNA) opened at the end of a 30-micron long metal-coated fiber tip. BNAs are gap-based nano-antenna[18] geometries known to confine and enhance electric optical fields[19-21]. However, as opposed to other gap antennas, a BNA has the ability to strongly reduce the background signal, which is of great practical interest in the development of a highly-sensitive fiber nanoprobe used in inhomogeneous diffusing media. Here, the BNA is placed at the end of a polymer tip serving as a tapered waveguide, efficiently matching radiation from the BNA to the fiber mode, and vice versa. Its rounded apex (with 500nm curvature radius) ensures propagation of the guided mode all the way to the end of the tip where the BNA is located[22], and vice versa. Viewing the BNA as an optical waveguide[23], the

tapered tip may be seen as an intermediate horn optical antenna which matches the electromagnetic fields of the BNA and the fiber guided mode[22]. The proposed hybrid combination BNA/fiber-tip leads to a highly efficient single-nano-antenna fiber probe, which remains effective even with relatively low fiber input powers or less-sensitive detectors.

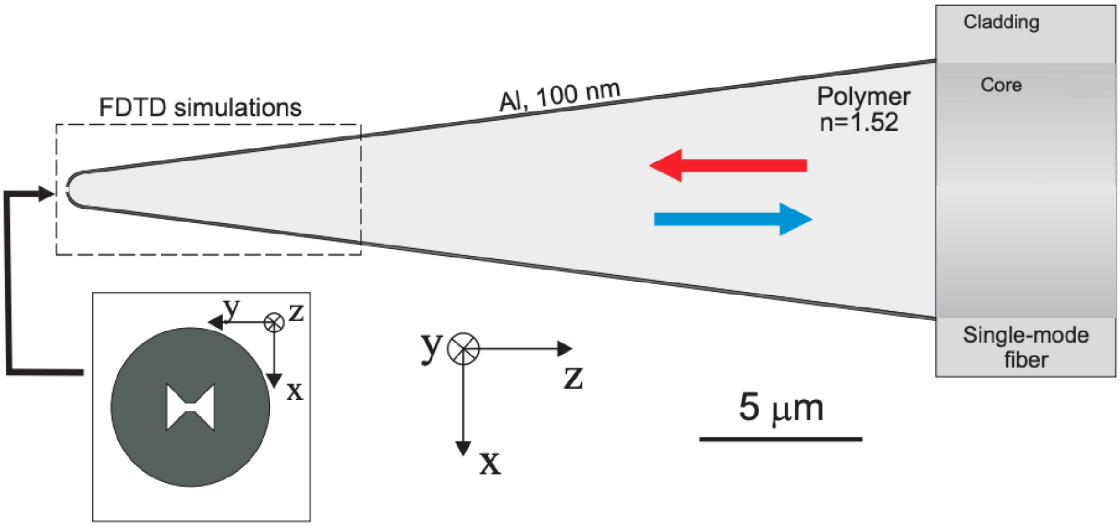

Figure 1.1. *Schematic of our bowtie nano-aperture on tip.*

To produce the BNA-on-tip, polymer tips (30µm long) are first grown by photopolymerization at the cleaved end facet of a monomode (1.55 µm wavelength) glass fiber[24]. Next, the probes are metal coated with a few nanometer thick titanium adhesion layer followed by a 100 nm thick aluminum layer. Aluminum is chosen for its high conductivity at infrared frequencies leading to a strong antenna effect[25]. Finally, a 210 nm wide BNA with square gap about 40 nm large and 45° flare angles is opened at the rounded apex of the tip by focused ion beam milling. Figures 1.2 a and b display scanning electron microscope (SEM) images of the fabricated result.

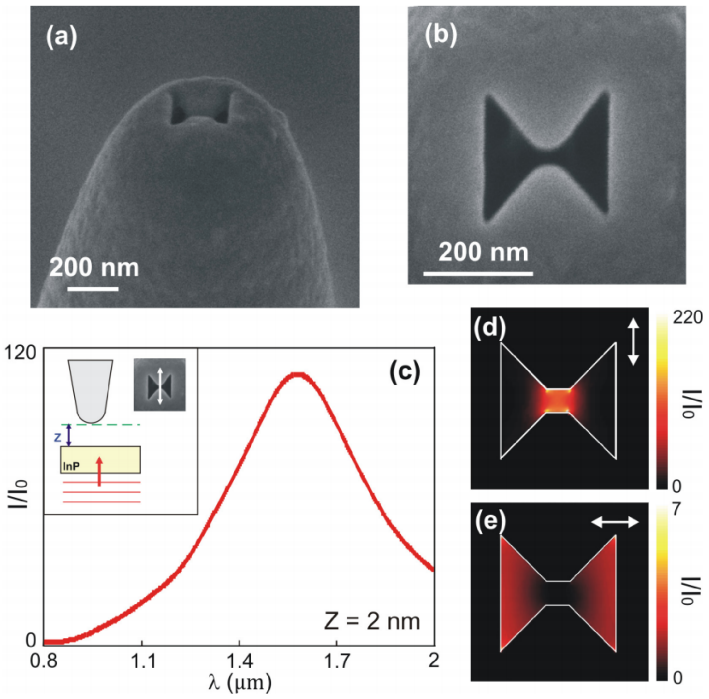

Figure 1.2. *SEM images of the BNA-on-tip: (a) side view and (b) top view of the tip apex. (c): theoretical resonance spectrum of the BNA-on-tip, positioned at a distance of 2 nm above an air/InP interface. The excitation plane-wave is incident from the InP substrate and is linearly polarized along the metal axis of the BNA (shown in the Figure inset). (d and e) Simulations of the electric intensity enhancement in a transverse XY plane taken at half the thickness of the metal layer and at λ = 1.59μm, for two perpendicular polarization directions of the incoming wave (see arrows).*

The BNA was designed to be resonant at λ = 1590 nm when it is in contact with an air/InP interface. The design process is performed using a three-dimensional Finite Difference Time Domain method (3D FDTD), and the permittivity of the metal (aluminum) is defined with a Drude model. Figure 1.2c shows the resonance spectrum of the BNA-on-tip placed at a distance Z = 2 nm away from a semi-infinite medium of InP in the air (see Figure inset). Note that the presence of this high-index medium has an influence on the resonance properties of the BNA (due to an effective surrounding index) and had to be taken into account in the design of the BNA. In the simulation, the BNA is excited with an incoming plane wave from the InP substrate (at normal incidence from the InP/air interface), polarized along the BNA's symmetry axis (see the white arrow of the Figure inset). The spectrum was calculated inside the BNA gap and normalized by the incoming field without the structure. The BNA resonance, of Q-factor about 3, is broad enough to allow high optical field enhancements in its gap zone at wavelengths ranging from 1450 nm to 1650 nm.

Figures 1.2d and e show the electric intensity enhancement simulated along the transverse (XY)-plane, which crosses the very tip at half the thickness of the metal layer, for an incident polarization (d) parallel and (e) perpendicular to the polarization axis of the nanostructure. We observe that the BNA's resonant mode, shown in Figures 1.2c and d, is strongly bound

to the nanometer gap. The electric field enhancement is induced by a resonant optical capacitive effect between the two closely spaced metal triangles of the BNA, leading to a charge distribution within the metallic arms that corresponds to an oscillating electric dipole[7]. The BNA's dipolar property, common to all gap-based nano-antennas, associates the generation of a small "hot spot" to high sensitivity to the polarization[26]. When the BNA is excited perpendicular to the gap orientation (see Figure 1.2e), the optical confinement is canceled, and the intensity maximum over the antenna is greatly reduced.
Moreover, since the localization and enhancement happen only at resonance[27], we expect that the collection efficiency of the BNA-on-Tip, which is several orders of magnitude larger than for circular aperture tips of the same opened area, will be driven by the electric field polarization in which the antenna is dipped[7,23].

1.2. Vectorial electric imaging of a photonic crystal laser cavity

To demonstrate the nanopolarizer capability of our probe in near field, the BNA-on-tip is coupled to a photonic crystal (PC) laser nanocavity, which consists of a linear defect of 7 cylindrical holes in a 2D triangular lattice[28] (holes period and radius of respectively 460 and 100 nm, see Figure. 1.3b). The two holes on both edges of the nanocavity are shifted by 80 nm outward in order to increase the Q-factor of the structure by 60% and thus achieve laser emission. The PC microlaser is fabricated into a 250-nm thick InP layer at the center of which are grown four InAsP quantum wells, separated by InP barrier layers. The photoluminescence from the quantum wells occurs between 1450 nm and 1650 nm. The heterostructure is bonded on the top of a transparent SiO2 substrate, allowing optical pumping from the backside and dissipating the heat production during laser emission. The PC is fabricated using e-beam lithography and reactive ion etching. The simulation of this nanocavity's optical properties with 3D-FDTD method reveals that the structure sustains several optical modes. However, the laser emission is often achieved only with the fundamental mode whose Q-factor (predicted to a value of 5800) is large enough to trigger population inversion within the active zone. The structure is designed so that its fundamental mode is resonant at λ = 1590 nm. The theoretical distribution of the electric intensity of the fundamental mode is plotted in Figures 1.3 c-e. Figure 1.3c reports the total simulated electric intensity, and Figures 1.3 d and e display, respectively, the intensity of the electric field components Ex and Ey, in near field.

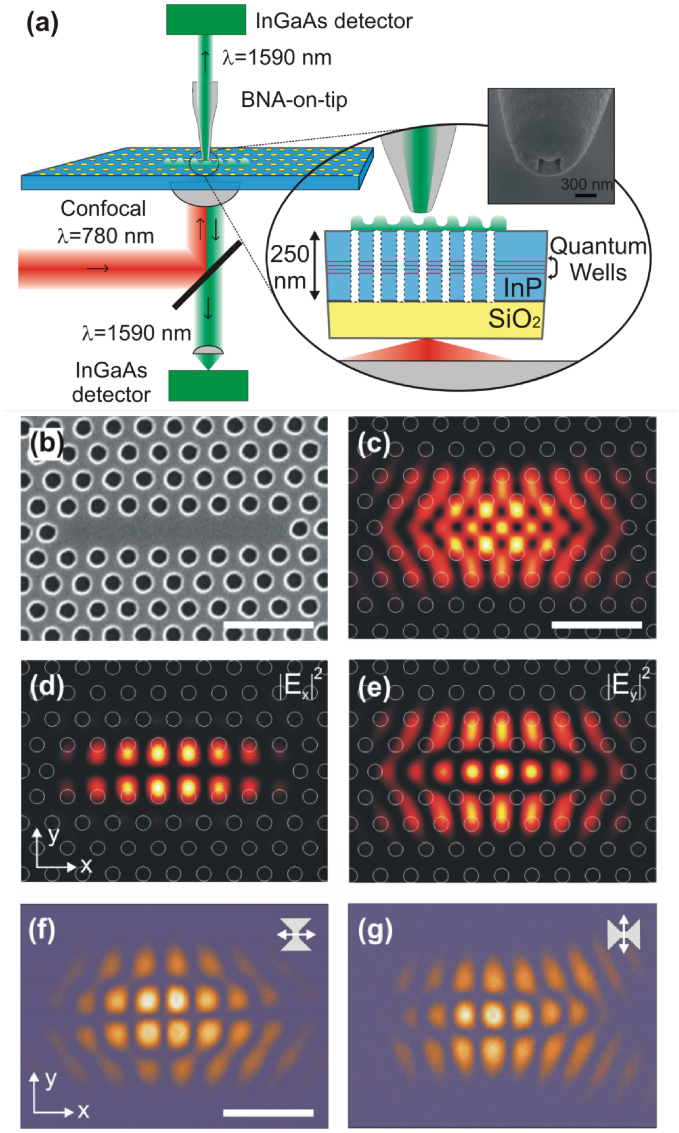

Figure 1.3. *(a) Schematic of the experiment. (b) SEM image of the PC nanocavity. (c-e) FDTD simulations of the structure's fundamental mode at λ = 1590 nm: (c) total electric intensity distribution, (d) intensity of the X electric field component (|Ex|²), (e) intensity of the Y electric field component (|Ey|²). (f and g) Near-field images of the PC laser nanocavity collected by the BNA-on-tip. The orientation axis of the BNA is (f) parallel and (g) perpendicular to the long cavity axis (see Figure inset). (scale bars: 1590 nm).*

The experimental set-up used in this study is shown in Figure 1.3a. The PC microlaser is pumped optically with a pulsed laser at λ = 780 nm (pulse width of 10 ns with a 5% cyclic ratio), and laser emission occurs at both sides of the InP layer. The pump is focused on the structure with a long working distance objective (x60, NA = 0.7) that leads to a spot size of about 3 microns. The BNA-on-tip is mounted onto a commercial NSOM to be positioned in the near-field of the PC. The near-field optical signal is collected locally by the BNA-on-tip and guided by the fiber to an InGaAs detector. The pump beam is filtered out, and a homodyne synchronous detection scheme is used to enhance the signal-to-noise ratio.

Figures 1.3 f and g report the images obtained by the BNA-on-tip during the scan of the PC for two orthogonal orientations of the antenna. By comparing Figure 1.3 d and f (Figures 1.3 e and g, respectively), we see that the BNA oriented along X (along Y, respectively) collects selectively the information carried by $|Ex|^2$ ($|Ey|^2$, respectively). The polarization sensitivity (measured experimentally to a value of 1:300 in intensity) unambiguously proves that the local collection process is driven by the optical capacitive effect that is resonantly excited within the nanometer scale gap of the BNA[7].

In conclusion, we have seen in this chapter that the field of investigation of optical nano-antennas has led to various applications related to nanophotonics. In particular, we have seen how a BNA antenna was sensitive to a single optical electric field component. Using this property, we have seen that such a nanostructure, placed at the end of an NSOM tip, allowed the collection of vectorial information related to the optical electric field in the near field. This characteristic has been used on a photonic crystal but can potentially be used on any optical nanostructures. Also, placing a photonic antenna at the end of a near-field tip has multiple applications, such as biological imaging[29] or optical trapping[11].

Papers related to this chapter :

Mivelle, M. *et al.* Bowtie nano-aperture as interface between near-fields and a single-mode fiber. *Opt. Express* **18**, 15964-15974 (2010).

Mivelle, M. *et al.* Light funneling from a photonic crystal laser cavity to a nano-antenna: overcoming the diffraction limit in optical energy transfer down to the nanoscale. *Opt. Express* **22**, 15075-15087 (2014).

Grosjean, T. *et al*. Optical horn antennas for efficiently transferring photons from a quantum emitter to a single-mode optical fiber. *Opt. Express* **21**, 1762-1772 (2013).

Ibrahim, I. A. *et al.* Bowtie-shaped nanoaperture: a modal study. *Opt. Lett.* **35**, 2448-2450 (2010).

Chapter 2

Plasmonic antennas to boost the magnetic light

We saw in the previous chapter that a plasmonic nanostructure could enhance the optical electric field by several order of magnitude[1]. In particular, due to a capacitive effect, a large electric field enhancement can be created within the air gap between two closely spaced metal nanoparticles. In this chapter I will describe, inspired by Babinet's principal, how a plasmonic nano-antenna is able to confine and enhance strongly the optical magnetic field as well.

Usually, ferromagnetic materials are used to strongly enhanced magnetic fields. However in the optical frequency regime we have to resort to other means in order to create enhanced magnetic fields. In the near-field, due to local interferences, the energy density of the electric and magnetic optical fields do not necessarily overlap, unlike in a propagating plane wave. Therefore, by nanostructuring matter, it is then possible to manipulate the spatial position of these energy density independently as well as modulate their intensities. For instance, the ability of some circular nanostructures to develop magnetic moments offers the possibility to locally enhance the magnetic optical near-fields. This was shown for example in the case of nanorings[30] and split ring resonators[31]. On the other hand, as shown in chapter 1, a strong electric field enhancement is created in the air gap between two closely spaced metal arms[7]. We saw that a bowtie nano-aperture (BNA)[17] was a very efficient nanostructure to create, confine and enhance the electric field at optical frequencies in the small gap between its two triangular tips. Inspired by Babinet's principle, we have proposed a new structure to enhance the optical magnetic field. Indeed, Babinet's principle states that the scattered electromagnetic field of an aperture ("negative" structure) in an infinitely thin perfect electric conductor is the exact same one than its complementary structure ("positive" structure) if the electric and magnetic fields are exchanged (mediating a opposite phase)[32]. Based on this principle, we numerically discuss in this chapter the near-field light components of the complementary BNA, which we have called the "diabolo nano-antenna"[33].

2.1. Principle of the diabolo nano-antenna

The geometry of the diabolo nano-antenna is shown in Figure 2.1a. Following Babinet's principle applied to the BNA, this structure consists of a pair of planar metal triangles connected together by a metallic junction. As it will be described below, a magnetic hot spot is generated at the junction when the incident electric field is linearly polarized along the y axis of the nano-antenna.

The basic principle of the diabolo nano-antenna originates from the electrical connection of two facing metal triangles, which in the BNA would be electrically isolated. The charge accumulation which occurs at the apexes of the two closely spaced metal triangles of the BNA (Figure 2.1b) is converted into a highly localized enhancement of the optical current

density along the metal junction (Figure 2.1c). The strong capacitive effect which drove the BNA and led to strong electric-field enhancement is changed to an inductive effect associated with a strong local enhancement of the magnetic field all around the metal gap. In fact, the metal triangles act as an electric funnel which reinforces the optical current density into the metal junction. Hence, following Ampere's law, we'll see that the magnetic field is azimuthally polarized around this central nanowire. We will see also that metal conductivity plays a crucial role in the performances of the diabolo nano-antenna since the strength of the electric current is related to the conductivity of the material.

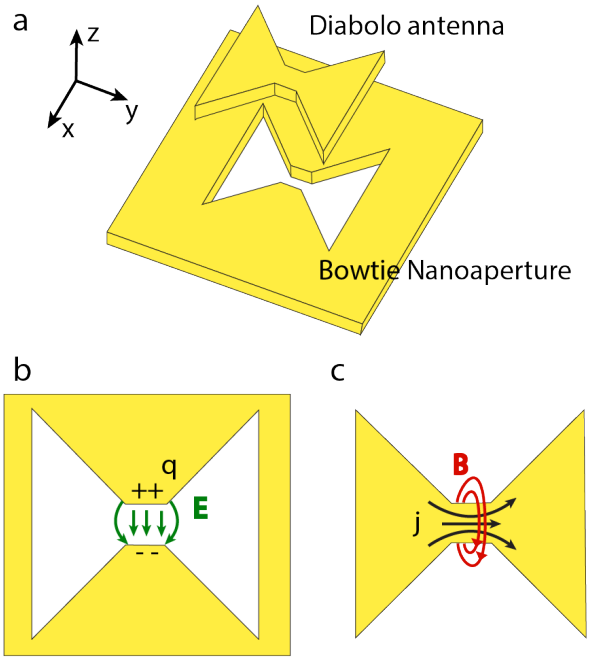

Figure 2.1. *(a) 3D view of the diabolo nano-antenna and its complementary bowtie nano-aperture. (b and c) Physical principles of the BNA and diabolo nano-antennas, respectively.*

2.2. Optical magnetic field enhancement

Using FDTD simulations, we numerically studied the optical response of the diabolo antenna.

The nano-antenna is placed onto a glass substrate (n=1.5) and illuminated with a plane wave propagating inside the substrate at normal incidence (Figure 2.2) with an electric field polarized along the y axis. A diabolo nano-antenna with 45° flare angles and a length D of 310 nm lies on the glass substrate. The electromagnetic response of the structure is studied for various metals (gold, aluminum, and silver), various sizes of the metal gap (G), and thicknesses of the nano-antenna (T). The permittivities of the metals are defined with a Drude model. Note that the height of the metal gap (along the z axis) is given by T whereas G defines both the width and the length of the metallic junction.

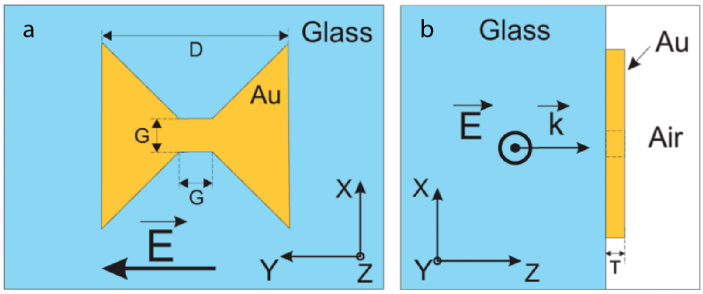

Figure 2.2. *Schematic of the studied antenna: (a) top view in the (XY) plane and (b) side view along the (XZ) plane.*

Figure 2.3 shows the near-field distributions of (a, b) the magnetic-field and (c, d) the electric-field generated by a gold diabolo nano-antenna at a wavelength of 1940 nm (at resonance). The structure under study is characterized by G=T=50nm and D=310nm. Intensity plots are given along (a, c) the longitudinal (XZ) and (b, d) the transverse (XY) planes. The (XZ) plane crosses the diabolo nano-antenna at the middle of the metal junction whereas the (XY) plane is taken 10 nm above the nano-antenna output plane, in air.
As anticipated, an enhanced magnetic field is highly confined all around the metal gap (Figure 2.3a,b) and is azimuthally polarized in the (XZ) plane (inset of Figure 2.3a). The enhancement of the magnetic intensity reaches a value of 230 at a distance of 10 nm away from the junction (Figure 2.3b) but becomes higher than 510 very close to the structure (Figure 2.3a). The enhancement of the electric intensity arises mainly at the end faces of the nano-antenna and is about 35 times smaller than the enhancement of the magnetic intensity at a distance of 10 nm beyond the metal gap and at the same position.

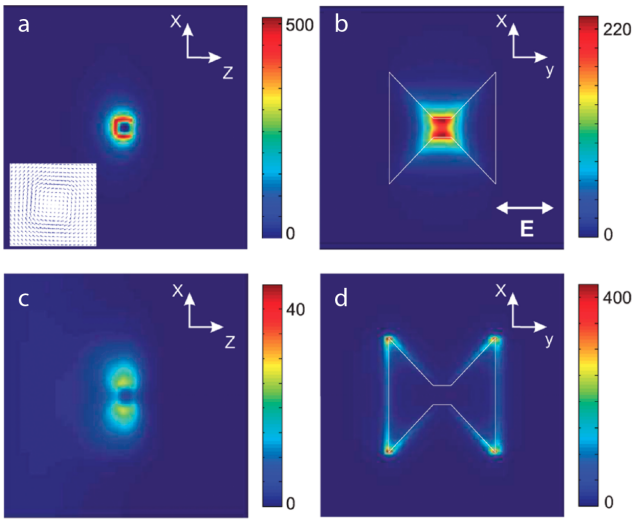

Figure 2.3. *(a-d) Normalized intensity distributions of (a, b) the magnetic field and (c, d) the electric field of a gold diabolo nano-antenna (G = T = 50 nm, D = 310 nm) excited with a plane wave whose electric field is linearly polarized along the y axis (λ = 1940 nm). Intensity plots along (a, c) the longitudinal xz plane and (b, d) along the transverse xy plane. Inset of (a): vectorial map of the magnetic field around the metal gap, in the xz plane.*

Figure 2.4a reports the magnetic spectral responses of various diabolo nano-antennas of length D = 310 nm and with parameters G and T equal to 50 and 50 nm (solid curve), 50 and 20 nm (dashed curve), 20 and 50 nm (dotted curve), and 20 and 20 nm (dashed-dotted curve). Figure 2.4b shows the magnetic response of the structure made of gold (solid curve), aluminum (dashed curve), and silver (dotted curve) for G = T = 50 nm and D = 310 nm.

Figure 2.4a shows that the cross-section area of the metal junction that is perpendicular to the current flow is the key geometrical parameter in the enhancement of the magnetic field. Any decrease in this area leads to an increase of the magnetic field and two geometries of the metal gap that lead to the same surface generate magnetic effects of the same level but not at the same wavelength (see dashed and dotted curves of Figure 2.4a). Thus, the maximum enhancement of the magnetic intensity, which is about 220 for a gold diabolo nano-antenna with G = T = 50 nm (Figure 2.3b), is enhanced by almost three times when G = T = 20 nm. Moreover, an increase of metal conductivity induces stronger current density in the structure and therefore higher inductive effect in the metallic junction. Figure 2.4b shows that the enhancement of the magnetic intensity is better for silver than for gold and aluminum, which have lower conductivities in the near-infrared region.

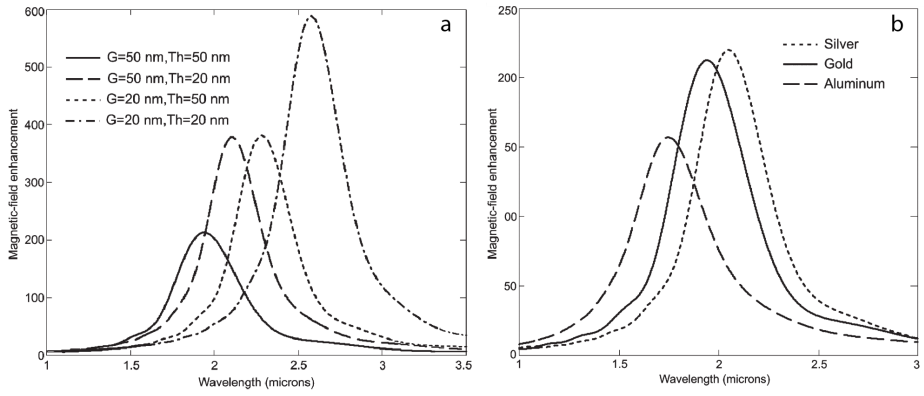

Figure 2.4. *(a) Comparison of the magnetic spectral responses of gold diabolo nano-antennas with D = 310 nm and G and T equal to 50 and 50 nm (solid curve), 50 and 20 nm (dashed curve), 20 and 50 nm (dotted curve), and 20 and 20 nm (dashed-dotted curve). (b) Magnetic spectral responses of diabolo nano-antennas made of gold (solid line), aluminum (dashed line), and silver (dotted line) with G = 50 nm, T = 50 nm, and D = 310 nm.*

In conclusion, from these results we understand that the underlying physics of the diabolo nano-antenna is that of a short-circuit between two oppositely charged metal bodies. Under illumination with an electric field polarized along the antenna y axis, charge accumulations of opposite signs arise at the end faces of the structure. These charge effects lead to high enhancements of the electric field on both sides of the diabolo nano-antenna, as shown in Figure 2.3d. The resulting potential difference between these two electrically connected metal structures generates currents which are guided across the metal junction. The double-funnel geometry of the diabolo nano-antenna concentrates and amplifies with high efficiency

the current density in the metal gap. Following Ampere's law, the resulting local increase of the current intensity leads to a strong enhancement of the optical magnetic field (as shown in Figures 2.3a,b).
We should mentioned that since this work has been published in 2011, other types of optical nano-antennas have been proposed to enhance strongly the optical magnetic field. We can mention the complementary of the bowtie nano-antenna (positive structure)[34] as well as dielectric nano-antennas[35-37]. In the later case, the nanostructures do not create strong conductive currents of course, but instead they drive high displacement currents, producing, in turn, a strong optical magnetic field. The following chapter will present such dielectric antenna.

Paper related to this chapter :

Grosjean, T. *et al*. Diabolo nanoantenna for enhancing and confining the magnetic optical field. *Nano. Lett.* **11**, 1009-1013 (2011).

Chapter 3

Photonic antennas designed by evolution

Light and matter interactions are often considered to be mediated by the optical electric field only, neglecting its magnetic counterpart.[38] This is particularly true in quantum optics, where the electric field couples much more strongly to the electric dipole of a quantum emitter than the magnetic field with the magnetic dipole (at least two orders of magnitude).[39-42] Nevertheless, increasing the magnetic energy density of light by several orders of magnitude with respect to the electric one would counterbalance the predominance of electric light-matter interactions. The potentiated occurrence of magnetic light and matter interactions would open up a new scope of possible applications in a variety of fields such as optoelectronics, nonlinear and nano-optics, spintronics, metamaterials, chiral optics,[43] sensing,[44] and photochemistry[45]. As we saw in the previous chapter, optical nano-antennas were recently proposed to boost the magnetic field of light in several theoretical studies[33,35,46-48], some of these structures were theoretically shown to strongly increase the emission rates of magnetic dipoles[8,42,46,49-55]. As well, experimental evidence for the capacity of optical nano-antennas to manipulate the emission of such dipoles at visible [56-60] or near-infrared[61] wavelengths has been brought about recently. In that context, based on Mie resonances, high index dielectric nanoparticles are of particular interest to efficiently enhance the magnetic optical field at visible wavelengths through strong displacement currents taking place inside these nano-antennas[53]. However, most of antenna designs suffer from the fact that the magnetic enhancement occurs inside the material, in the core of the structures, making it difficult to access the hotspot experimentally and use its full potential[62]. Hollow nano-disks[52,54,55] (i.e nanocylinders) were proposed to overcome this hurdle, granting access to the magnetic field that would be partially enhanced in air and not entirely in the dielectric material. However, it is still very challenging to place a nanoscale piece of material inside hollow nanodisks, making nanostructures featuring easily accessible magnetic hotspots particularly appealing. Along those lines, it was recently demonstrated that evolutionary algorithms[63] can produce optical nanostructures behaving far better than conventional photonic antennas[64-66] or devices[67-71]. By coupling the power of computation algorithms to specific goals and the intuition of researchers, these approaches are redefining what might be the future of nanophotonics.[63]

In this chapter, I will describe how evolutionary algorithms are a powerful alternative to design dielectric optical nanostructures able to strongly enhance the optical magnetic field of light at visible wavelengths, in the near field[72]. Furthermore, while dielectric nano-antennas usually create a magnetic field hotspot inside the material (i.e. inside the antenna), the architectures we developed feature a reachable magnetic field just above the antenna, with up to 5 times more enhancement than hollow nanodisks. I'll finally describe that, although algorithmically optimized geometries are more elaborate than the shape of conventional nano-antennas, their photonic response depends very weakly on the fine details of the design. In fact, a rough fabrication process following the general shape of the optimized

antenna would still lead to more than a 4 times enhancement of the optical magnetic intensity with respect to state-of-the-art nano-antennas, highlighting the feasibility of their experimental implementation.

3.1. Description of the Genetic Algorithm

Numerical evolutionary algorithm techniques mimic the natural selection processes that happen during the evolution of species. Figure 3.1a summarizes this approach for the design of silicon-based nano-antennas featuring enhanced magnetic fields. First, a population of random nanostructures is generated. Then, each population is evaluated for our specific goal through Finite Difference Time Domain (FDTD) simulations, in order to obtain the highest optical magnetic intensity at a targeted location in the near field of the nanostructure. From this analysis, we select the antennas that provide the best results and we create a new population by either mutating or breeding these selected designs. This second generation is then evaluated again through FDTD, and so on until, after several generations, an optimized solution emerges. In here, each population is composed of 20 elements and each new generation is elaborated from the 5 best structures favored during the selection process. Each element of each generation is reduced to a 11x11 binary matrix made of 0 and 1[64], as shown in Figure 3.1b, and each 1 of this matrix corresponds to a parallelepiped made of silicon in the FDTD simulation, while each 0 corresponds to air. The center of these silicon blocks is then placed in an array with a periodicity of 30 nm in x and y inside the FDTD simulation. At first, the x and y dimensions of the silicon parallelepipeds are set to 40x40 nm^2, a dimension slightly larger than the periodicity in order to have overlapping blocks of silicon at certain places, allowing displacement currents to emerge inside the dielectric material of the antenna. An example of the corresponding structure associated to the matrix in Figure 3.1b is displayed in Figure 3.1c. The full width D in Figure 3.1c was set to 340 nm. The thickness h of the structure was 110 nm (Figure 3.1d), in order to ensure a π phase shift of the incoming plane wave between the entrance (lower part) and the exit (top part) of the silicon elements (for an optical index of the silicon obtained experimentally[58]). This condition is usually required for dielectric Mie resonators used to enhance the magnetic optical field[62], which led us to use it as a starting point in the simulations. The nanostructure was illuminated in normal incidence by a plane wave, 600 nm in wavelength and circularly polarized. The maximization of the magnetic intensity was then investigated just above (in the first mesh cell in z), and in the centre (x,y) of the structure (red spot in Figures 3.1c and d).

The FDTD method is time consuming and requires high computational power. Therefore, in order to speed up the selection process, we first used a rough discretization mesh of 10x10x10 nm^3 in size to describe the binary matrices in the simulations. For the same purpose of saving computation time, the simulations were stopped after 10 optical cycles, a number that is sufficient to reach a plateau in the optical response of the simulated nanostructures.

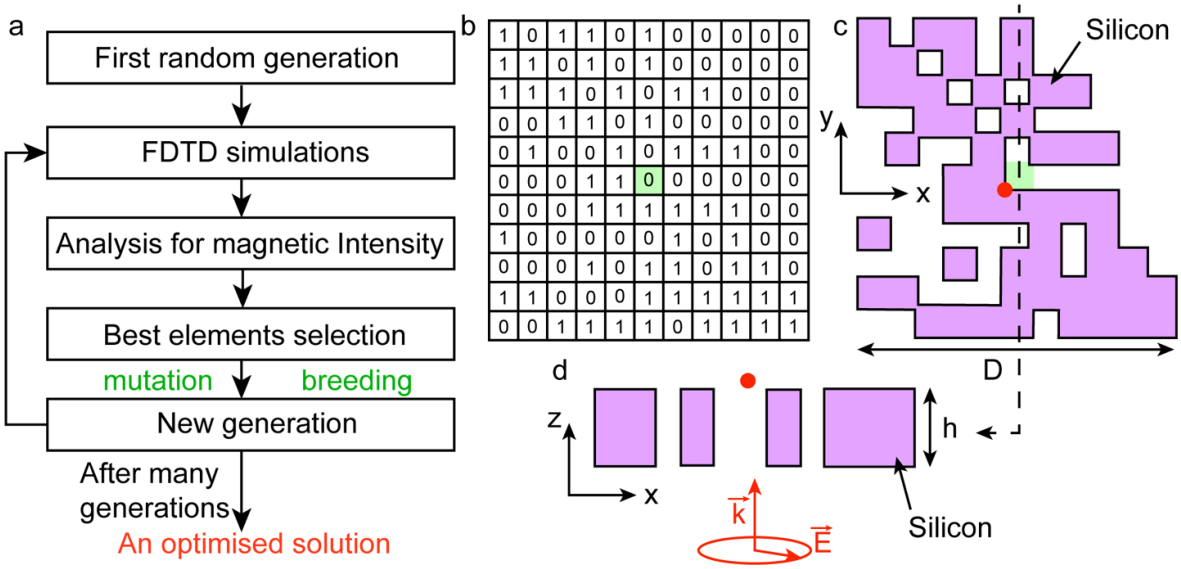

Figure 3.1. *General concept of the genetic algorithm (GA) developed for designing nanostructures that optimize local magnetic fields. (a) Schematic of the different steps realized during the selection process. First, a random generation of 20 elements is created, and each of these elements is evaluated through Finite Difference Time Domain (FDTD) simulations. The 5 structures giving the highest magnetic field intensity are selected and 20 new elements are created by either mutating or breeding the 5 selected elements. This new generation is then evaluated through FDTD again until, after several generations, an optimized solution emerges. (b) Typical binary matrix defining a structure to be evaluated: each 1 corresponds to a silicon parallelepiped in the FDTD simulation. (c) Schematic representation, in the (x,y) plane, of the structure produced by the matrix in (b), (D = 340 nm). (d) Cross section of the structure in (c), in a (x,z) plane (indicated by the dashed line in (c), (h = 110 nm). The nanostructures are excited by a plane wave, at λ=600 nm, with a circular polarization and propagating in a direction normal to the (x,y) plane. The red spot in (c) and (d) corresponds to the position where the magnetic intensity enhancement is evaluated (the first mesh cell above the structure).*

3.2. Genetic Optimization of a Dielectric Antenna

Taking into account all these parameters, Figure 3.2a displays the typical optical magnetic field intensity enhancement in the center (x=y=D/2, z=h+5 nm) of the generated structures during the evolutionary process. In here, each data point represents a single simulation of a unique nanostructure. Each generation is therefore composed of 20 data points, meaning that more than 7000 independent simulations are presented in Figure 3.2a. As we can see, the magnetic field intensity enhancement quickly increases with the number of generations, reaching a plateau after about 150 successive mutations of the nanostructure geometry. Figures 3.2b and d show 2 structures at different steps of the evolutionary process, at respectively generation 50 and 100. We observe that the central shape is maintained already from a very early point onwards in the selection process,

suggesting an important role in the magnetic field intensity enhancement. In addition, Figures 3.2c and e display the magnetic field intensity enhancement of the structures presented in Figures 3.2b and d, respectively. We notice that the magnetic intensity distributions are rather similar in shape but with a higher confinement and enhancement in the case of generation 100, indicating that the changes at the periphery of the structure from generation 50 to 100 resulted in a high concentration of the magnetic energy density and therefore to a higher intensity enhancement.

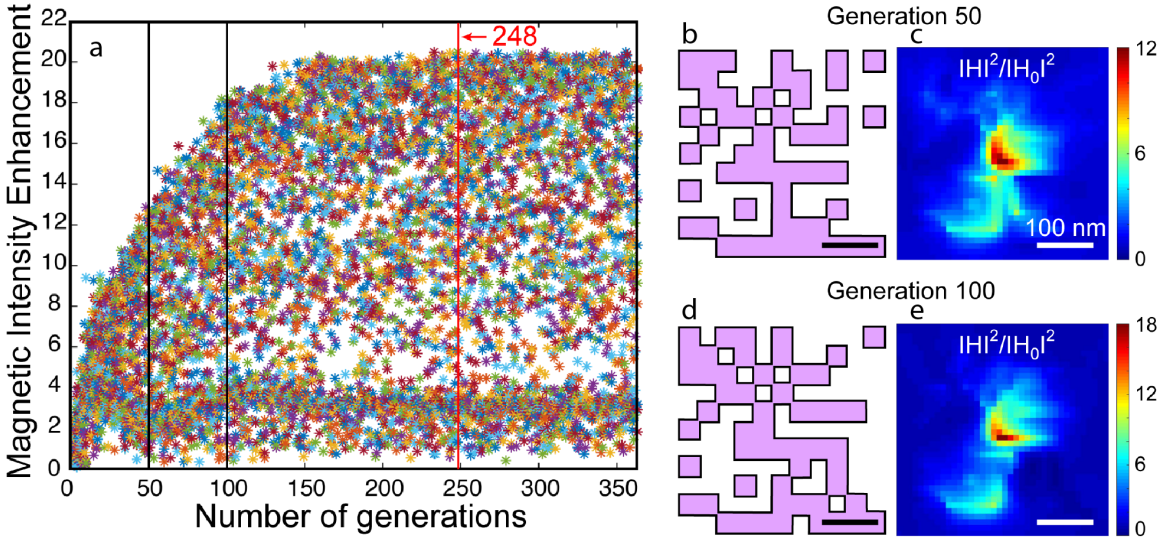

Figure 3.2. *Magnetic field intensity enhancement during the evolutionary process. (a) Magnetic intensity enhancement in the centre of the nano-antenna (red point in Figures 3.1(c) and (d) versus the number of generations. Each generation displays the results of 20 structures (20 data points), characterizing the extending increase of the magnetic intensity for each generation. (b) Optimal structure at generation 50 and (c) corresponding magnetic intensity enhancement distribution in a plane 5 nm above the silicon (z=115nm). (d) and (e) Optimal structure and distribution of the magnetic field intensity increase, in the same plane as (c), at generation 100.*

3.3. Behavior of the Optimized Antenna

From Figure 3.2a, we were also able to identify the design with the highest magnetic field enhancement selected by the algorithm, which was found to be at generation 248 and is presented in Figure 3.3a. In order to better describe the behavior of that specific structure, the mesh of the simulation was then changed to 2x2x2 nm^3 and a second optimization allowed by this fine mesh was performed, consisting in changing the aspect ratio (global size of the antenna), the thickness and the sizes of the parallelepipeds made of silicon. The final structure was then found to be made of parallelepipeds of silicon with dimensions of 36x36 nm^2 in (x,y) and 92 nm in z, surrounded by air and positioned with a periodicity of 33 nm in x and y, with a total width D of 366 nm. This nanostructure was then compared, in the same conditions and using the same materials, to a hollow nanodisk[52,55], the best silicon nano-

antenna that was known so far with both high enhancement and good accessibility of the field.

Figures 3.3c and d display the magnetic intensity enhancement 2nm above the GA design and the hollow nanodisk, respectively. Although the reduction of the mesh size slightly lowers the magnetic field intensity enhancement, we can see that the GA reaches a magnetic energy density that is five times higher than that of the hollow nanodisk, demonstrating the potential of evolutionary algorithms to generate accessible hot spots of the magnetic field only.
Apart from the magnetic enhancement, the ratio between the magnetic and electric field intensity is also an important feature for an effective magnetic antenna. Figures 3.3e and f display the normalized electric field intensity and the ratio between magnetic and electric normalized intensities, respectively, in the same plane as Figure 3.3c. From these distributions, we see that the electric and magnetic field do not overlap in the near field of our GA design. In addition, we can observe that, at certain positions, the ratio of magnetic over electric intensities is very high (more than 80). It is worth noticing that such a genetic algorithm could equally be used to optimize this relative magnetic / electric ratio instead of optimizing the magnetic field enhancement. This would be of particular interest to specifically study the coupling between magnetic light and matter with a very high efficiency and without competition from the electric optical field.

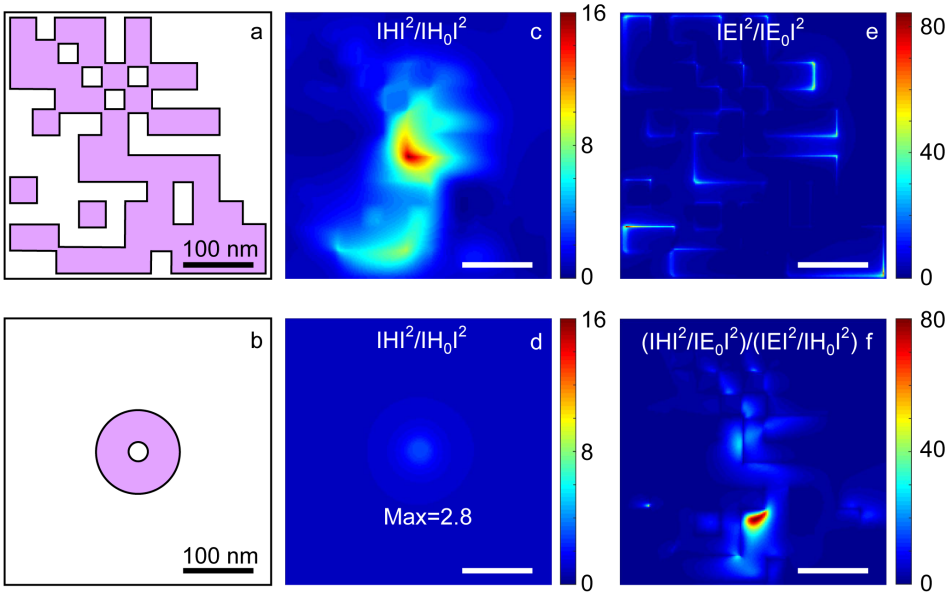

Figure 3.3. *Optimized structure and comparison with a hollow silicon nanodisk. (a) Optimized structure obtained after 248 generations and (c) distribution of the magnetic intensity enhancement of (a) 2nm above the top plane of the antenna in z. (b) Schematic of a silicon hollow nanodisk, that was considered at that time as the best dielectric nano-antenna allowing an accessible magnetic hot spot and (d) corresponding magnetic intensity increase produced by (b), 2nm above the antenna in z as well, and with a maximum of 2.8. e) Electric field intensity enhancement distribution in the same plane as (c). (f) Magnetic over electric intensity enhancements in the same plane as (c) and (e).*

3.4. Influence of Low Structural Details on the Behavior of the Optimized Dielectric Antenna

Since GA designs are more elaborate than commonly studied optical nano-antennas, their experimental nanofabrication can be challenging. To provide insights towards this issue, we created a new nanostructure, shown in Figure 3.4a, used as an extreme case in which the sharp edges of the design, which are challenging to fabricate, are modified. This rough design follows the general shape of the optimized structure in Figure 3.3a, but instead of using parallelepipeds made of dielectric or air, we perforated a block of silicon with dimensions of 366x366 nm^2 in (x,y) and 92 nm in z, by cylinders made of air with diameters of 38 nm and a height of 92 nm. The magnetic intensity distribution produced by this rough design that would be significantly easier to fabricate by focused ion beam milling or e-beam lithography, is shown in Figure 3.4b. Comparing the rough structure with the original structure, we can observe that the spatial distribution of the magnetic intensity is almost not affected by changing the sharp edges, and the intensity enhancement is slightly lowered, but is still significantly larger (more than 4 times) than the enhancement recorded above a hollow nanodisk (Figures 3.3b and d). This result indicates that once the general GA design is defined, the fine details should only contribute marginally to the field enhancement, increasing the compatibility of the GA designs with experimental nanofabrication.

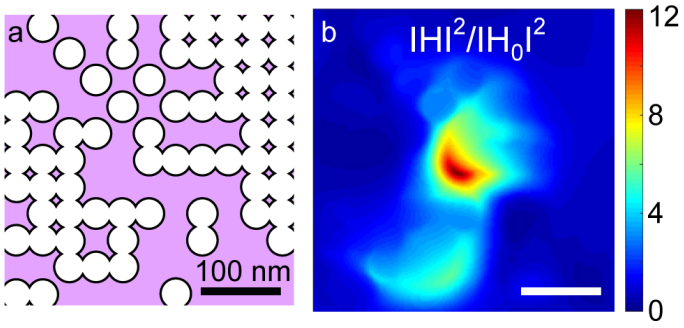

Figure 3.4. *Low detailed design structure. (a) Schematic of an optical nano-antenna where the parallelepipeds of air are replaced by cylinders of 38 nm diameter in the optimized GA design, in order to render the effect of a low detailed structure. (b) Magnetic intensity enhancement of a in a plane 2 nm away in z from the antenna.*

In conclusion, I have described you how evolutionary algorithm approaches are a powerful tool for designing dielectric optical nanostructures, and are able to enhance the magnetic intensity of light 5 times more than what state-of-the-art photonic nano-antennas was allowing at that time. Furthermore, together with the fine-tuning of the optimized design, we saw that although GA designs are more elaborate than most of the optical nano-antennas known so far, the optimized shape is weakly dependent on fine structural details (such as sharp edges), and that a rough nanofabrication process would still lead to a much larger enhancement of magnetic field intensities than hollow nanodisks. I believe that this approach will lead to a leap forward in the design of optical nanodevices to study and increase the

coupling between magnetic light and matter. In addition, I envision a broad application of the GA approach by setting different selection criteria, such as maximizing the ratio between magnetic over electric intensities, or setting multiple selection criteria at once, and by using alternative materials or wavelengths. In particular, the use of plasmonic materials should be of interest to enhance the magnetic field at near-infrared telecommunications wavelengths, where erbium ions exhibit strong magnetic dipolar emission.[73]

Paper related to this chapter :

Bonod, N. e*t al*. Evolutionary Optimization of All−Dielectric Magnetic Nanoantennas. *Advanced Optical Materials* **7**, 1900121 (2019).

Bidault, S. *et al*. Dielectric nanoantennas to manipulate solid-state light emission. *J. Appl. Phys.* **126**, 094104 (2019).

Part 2. Coupling of electric light and matter through a photonic antenna

In this part, we will see through chapters 4 and 5 the manipulation of the emission of fluorescent molecule-type quantum emitters via an optical nano-antenna. In the first chapter (chapter 4), I will describe a new type of photonic antenna based on the hybridization of two well-known antennas, the bowtie nano-aperture, and the monopole antenna. We will see how this antenna makes it possible to image single fluorescent molecules with a resolution of about twenty nanometers, a position accuracy lower than one nanometer, and this in a multicolor fashion. The research in this chapter was carried out at the ICFO institute in Barcelona in the group of Maria Garcia Parajo, in the framework of a European project bringing together biologists from Nijmegen, researchers from EPFL, the Fresnel institute in Marseille and ICFO. The aim of this project was to develop photonic nanoantennas for the study of living cells. In particular, by combining the properties of antennas to focus light together with fluorescence correlation techniques, this project had the ambition to study the dynamics of single membrane proteins and their interactions. These antennas had to be able to be used directly on a substrate or at the end of a near field tip. My thesis work was thus well suited to these studies.
In a second chapter (chapter 5) we will also see how the same antenna allows us to manipulate the non-radiative energy transfer between two quantum emitters by modifying the local density of states sensed by the quantum emitter from which the energy transfer originates. Indeed, one of the researchers of the Fresnel Institute involved in the European project, Jérôme Wenger, was also awarded an ERC project whose goal was to increase the non-radiative energy transfer between quantum emitters. As his project and ours overlap on several domains or experiments, it is quite naturally that I became interested in the manipulation of these non-radiative transfers via optical nanostructures. This led to the study described in chapter 5 and whose idea came to me when I was still a post-doc in Barcelona. It was then realized by Maria Sanz, a PhD student I was supervising in ICFO.

Chapter 4

Broadband Single fluorescent molecules imaging by a photonic nano-antenna

Modern far-field super-resolution methods are offering unique capabilities for probing biology at the nanoscale by fluorescence[74-78]. In general, these techniques rely on the controlled switching of the sample fluorescence emission in time, either spatially[79] or stochastically[80-82], providing resolutions or localization accuracies in the 30-80nm range[74,75]. More recently, single-color localization precision down to few Angstroms has been demonstrated by stimulated emission depletion using ultra-stable emitters[83]. In biologically relevant samples, dual-color localization methods recently showed accuracies up to 7.5 nm under highly controlled experimental conditions[84]. True optical nanoscale resolution without relying on sample´s properties can alternatively be obtained by interacting with emitters in the near-field, as earlier demonstrated using near-field scanning optical microscopy (NSOM)[85]. Unfortunately, although NSOM can in principle provide unlimited multicolor spatial resolution, the low throughput of subwavelength aperture NSOM probes limits in practice the resolution to ~50-70nm[86]. We have seen in the previous chapters that optical antennas have emerged as excellent candidates to amplify electric fields into localized nanometre-scale regions[1,6,7,10,87,88]. When fabricated at the apex of scanning probes, these devices allow full three-dimensional (3D) control for positioning the antenna in proximity to single emitters offering ~30nm single-color optical resolution[6,89].

In this chapter, I will describe a novel hybrid nano-antenna probe that overcomes these limitations affording truly background-free broadband nanoimaging of individual fluorescent molecules[90]. The architecture of the device and its mechanical stiffness allows simultaneous operation for shear-force topographic and multicolor imaging with identical spatial resolution. We performed dual-color nanoimaging of individual molecules at high concentrations demonstrating optical resolutions of ~20nm. The spectral separation, extreme spatial light confinement and high single-molecule photon signals enabled direct discrimination of close-by molecules separated by 2.1 nm together with Angstrom precision. Importantly, compared to far-field super-resolution methods our engineered antennas do not rely on the sample fluorescent properties, adding extra flexibility on the choice of fluorescent probes for multicolor nanoimaging and being fully compatible with live cell research.

4.1. A hybrid photonic antenna

Our device consists of three optical elements (Figure 4.1a). A metal-coated tapered optical fiber with a well-defined glass opening (500−700 nm) guiding the incoming light to a bowtie nano-aperture antenna (BNA). The BNA combines high transmission and strong mode confinement at the gap region under transversal polarization (aligned across the gap)[91], as shown in chapter 1. A monopole nano-antenna is further engineered at one of the edges of the BNA gap affording efficient light coupling from the bowtie gap to the monopole with a

spatial confinement determined by the radius of curvature of the monopole tip end. The device was fabricated by focused ion beam (FIB) reaching ~85% reproducibility for radius of curvatures of the monopole tips between 15-30nm (Figure 4.1b). Since the monopole nano-antenna is excited at the back end of the fiber and fully integrated in a single block, i.e., progressively carved on the optical fiber, there is no light leakage associated with far-field excitation of the structure: only the near-field light at the monopole end interacts with the sample. Moreover, high far-field to near-field coupling efficiency is achieved, only limited by the losses on the fiber tapered region which are minimized by matching the tapered end diameter to the excitation wavelength, in the same way than the polymer tip of chapter 1. For operation as nano-light illumination source, the hybrid nano-antenna is mounted on a scanning probe holder coupled to an inverted confocal microscope optimized for dual-color single molecule fluorescence detection (Figure 4.1c). The antenna is maintained in proximity to the sample surface (~20nm) using a shear-force distance control as commonly used for NSOM. This allows full 3D positioning control of the antenna with respect to the sample while providing simultaneous topographic images similar to those obtained using atomic force microscopy.

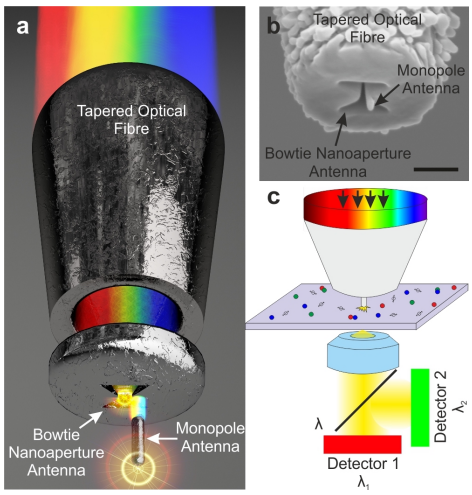

Figure 4.1. *Hybrid nano-antenna probe for dual color single molecule nanoimaging. (a) Schematics of the hybrid nano-antenna probe decomposed in the three main elements: a tapered optical fiber coated with 150nm of aluminium, the BNA carved at the aluminium-coated end facet of the tapered fiber, and the monopole nano-antenna positioned at one of the edges of the BNA gap. (b) Scanning electronic microscopy (SEM) image of a fabricated hybrid nano-antenna probe. Scale bar: 300 nm. (c) Sketch of the experimental setup. The antenna is mounted on a NSOM head holder and aligned with respect to the optical axis of the microscope. The antenna-sample separation (~20nm) is controlled using a shear-force feedback system. The antenna is excited by coupling the light to the back end of the optical fiber. Polarization and power injected to the fiber is adjusted independently for each wavelength. The sample is scanned with respect to the antenna using a close-loop feedback system. The emitted fluorescence is collected by a x100, 1.3 NA immersion-oil objective focused at the sample/tip plane, separated from the excitation light, split into two branches according to the emission wavelength and detected by two single photon counting avalanche photodiodes (APDs).*

We performed FDTD simulations to estimate the near-field intensity profiles in the xy-plane at 10 nm away from the monopole tip. Figures 2a, b show the intensities at the apex of a 30nm monopole tip (E_{tot}^2) normalized by the intensity launched in the simulation (E_0^2) when the BNA is excited under transversal (Figure 4.2a) and longitudinal polarization (Figure 4.2b). For transversal polarization the field is confined at the BNA gap region[91] and efficiently excites the monopole resulting in large field enhancement and confinement (Figure 4.2a). For longitudinal polarization there is no enhancement at the BNA gap and the monopole antenna is not excited (Figure 4.2b). To validate these simulations we imaged 20 nm fluorescent beads immobilized in a thin polymer (PVA) film using a hybrid antenna probe with a tip curvature diameter of ~ 55nm excited at λ=633nm. Figures 4.2c,d shows the fluorescence emission of the same bead for transversal (Figure 4.2c) and longitudinal BNA excitation (Figure 4.2d). The excellent agreement between simulations and experiment confirms that the confined field at the BNA gap region determines the effectiveness of the coupling between the external laser and the monopole antenna. Experimentally, we measured confinement of (67±4) nm in xy-directions and a signal-to-background (S/B) ratio of 70 for transversal BNA excitation (Figures 4.2e,f), while a much weaker and spatially dispersed fluorescence pattern was obtained for longitudinal BNA excitation (Figures 4.2e,f). The somewhat modest enhancement obtained upon BNA transversal excitation as compared to simulations is mainly due to the larger monopole radius and larger tip-sample separation distance used in the experiments.

We further assessed the spectral response of hybrid nano-antennas as a function of the monopole length for transversal excitation polarization. Coupling between the BNA and the monopole leads to a large broadband response in the visible range that weakly depends on the monopole length (Figure 4.2g). The highest intensity is around 650nm corresponding to the wavelength of maximum transmission of the BNA[91] for hybrid nano-antennas with monopole lengths between 50-70 nm. For longer monopole lengths a red shift of the spectral response is observed, an effect due to its λ/4 character[6].

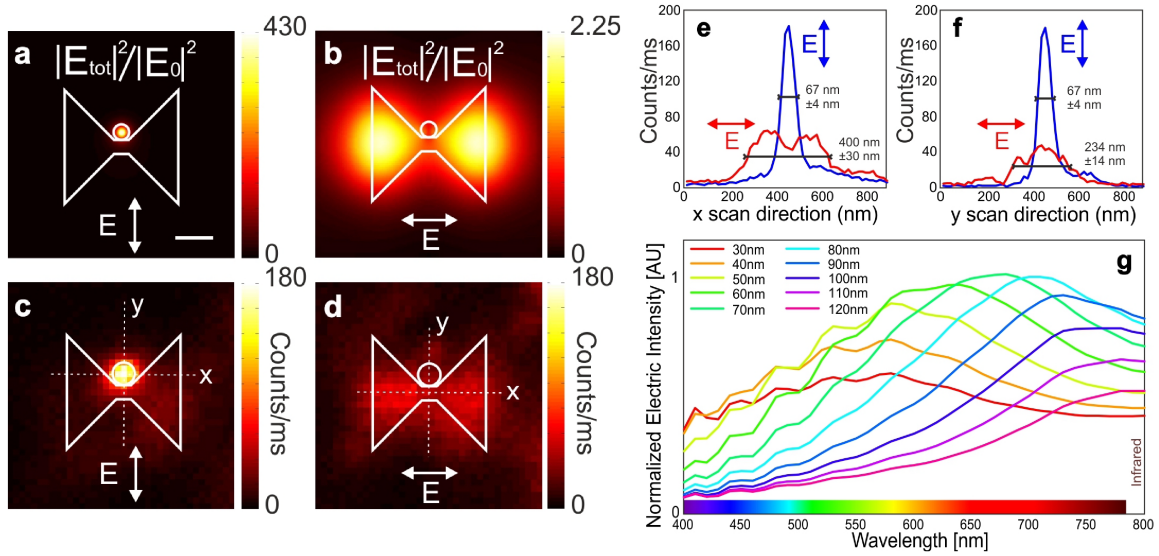

Figure 4.2. *Near-field FDTD simulations and experiments of the hybrid nano-antenna. (a,b) Normalized intensity (E_{tot}^2/E_0^2) calculated in a xy-plane at 10 nm away from the monopole tip, for transversal (a) and longitudinal (b) excitation polarization (λ=633 nm) of the BNA. The BNA gap is 30 nm, the monopole length is 70 nm with tip diameter of 30 nm. (c,d) Near-field images of a 20 nm fluorescence bead scanned under the hybrid nano-antenna upon transversal (c) and longitudinal (d) BNA excitation at λ=633 nm. Images consist of 38 x 38 pixels, pixel size: 15.6 nm, recorded with a dwell time of 5 ms. The length of the monopole is 65nm and tip diameter is 55 nm. (e,f) Fluorescent line profiles along the x-(e) and y-(f) scanning directions as taken from Figure 4.2c,d (see dashed lines) for transversal (blue) and longitudinal (red) BNA excitation. (g) Spectral intensity response of the hybrid nano-antenna under transversal excitation for different monopole lengths.*

4.2. Multi-color nanoscale imaging and subnanometric localization

As a first practical test of the broadband nanofocusing performance of the device we prepared a sample composed of different color beads (⌀=20 nm) immobilized in a thin PVA layer. The sample was scanned under a hybrid antenna excited simultaneously by two laser beams (λ=488 nm and λ=633 nm, transversal polarization). Figure 4.3a shows a 3D projection of simultaneously obtained topography and dual-color imaging of the fluorescent beads. The height of the beads ranges from 8 nm to 20 nm depending on how much they protrude out of the PVA layer. Importantly, the simultaneously obtained images show a direct correlation between the beads topography and their fluorescence emission (dashed lines in Figure 4.3a). Line scans over two different color beads indeed show perfectly overlaid equal topography and dual-color optical resolution with a full-width-at-half-maximum (FWHM) of ~80 nm (Figures 4.3b,c). These results demonstrate that the dual-color near-field excitation is concentrated at the tip end of the monopole, serving also as a sharp and mechanically robust tip for topographic nanoimaging.

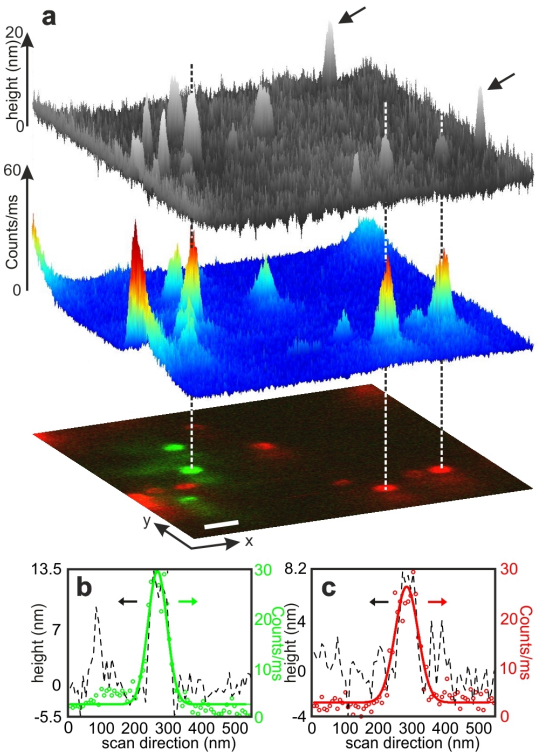

Figure 4.3. *Correlated topography and dual-color imaging using a hybrid nano-antenna probe. (a) 3D projection of a simultaneously obtained topography (grey) and dual color intensity image (jet) of multicolor fluorescent beads of 20 nm in diameter. The image beneath the 3D projection corresponds to the dual color image, where green corresponds to beads excited at λ=488 nm and detected at (520±16) nm, and red corresponds to beads excited λ=633 nm and detected above 672 nm. Dashed lines illustrate the perfect overlay between topography and fluorescence signal. Notice that some topographic features (black arrows) do not have associated emission, probably corresponding to topographic impurities on the sample. Images have been recorded with a hybrid nano-antenna having a tip diameter of 70nm and 60nm length, simultaneously excited with two laser beams (λ=488 nm and λ=633 nm, transversal polarization, 50 μW). Scan step size: 7.8 nm, dwell time: 3.33 ms. Scale bar: 200 nm. (b,c) Lines profiles (topography, left axis; fluorescence, right axis) of two representative beads.*

A more severe resolution and sensitivity test was pursued by imaging a highly dense (10^{-6}M) sample of mixed (DiD and DiI) fluorescent molecules embedded in a thin PMMA layer. Excitation was provided in confocal fashion or by the hybrid nano-antenna using simultaneously two laser beams (λ=560 nm and λ=633 nm). Although the confocal image (Figure 4.4a) appears overcrowded due to diffraction, the near-field image (Figure 4.4b) clearly resolves individual molecules in two colors with similar brightness and resolution. Lines profiles over two different individual molecules (DiD and DiI) show FWHM optical resolutions (~20±2) nm (Figures 4.4c,d). Importantly, the large and confined excitation field provided by the hybrid nano-antenna renders single molecule signals of ~2.5-3x10^5 photoncounts in 1s and typically 10^4 photoncounts/spot.

The spatial xy-coordinates, i.e., localization precision, of each single molecule can in principle be calculated by taking into account the effective spot width, the number of collected photons and the background. In the near-field regime, this estimation must however be performed with cautious since the orientation of the emitter´s dipole moment relative to the antenna can influence the lateral position at which the fluorescence spot is observed, an effect that strongly depends on the molecular orientation, the antenna-emitter coupling strength and their separation distance[15,92]. Although we did not record the orientation of the molecules, this effect is estimated to be minor in our experiments given the broadband response of our antennas, i.e., weak antenna-emitter coupling, and the relatively large tip-emitter separations used (~20nm)[93]. Yet, to rule out any potential influence on the localization precision determination, we restricted our analysis to those near-field fluorescence spots having well-defined circular patterns, mostly arising from out-of-plane oriented molecules[15,92]. With a spot width of ~20 nm and 10^4 photoncounts/spot (after background subtraction) the localization accuracies retrieved are within 2-2.5 Å, i.e., three-orders of magnitude below the diffraction limit or λ/3150 (Figures 4.4e,f). This extraordinary improvement in localization accuracy is also illustrated in Figure 4.4g where the xy-molecular coordinates of the individual molecules mapped by the hybrid nano-antenna are plotted. It is worth mentioning that in principle all molecules can be determined with similar extreme localization accuracy provided that their orientation and distance from the antenna are known.

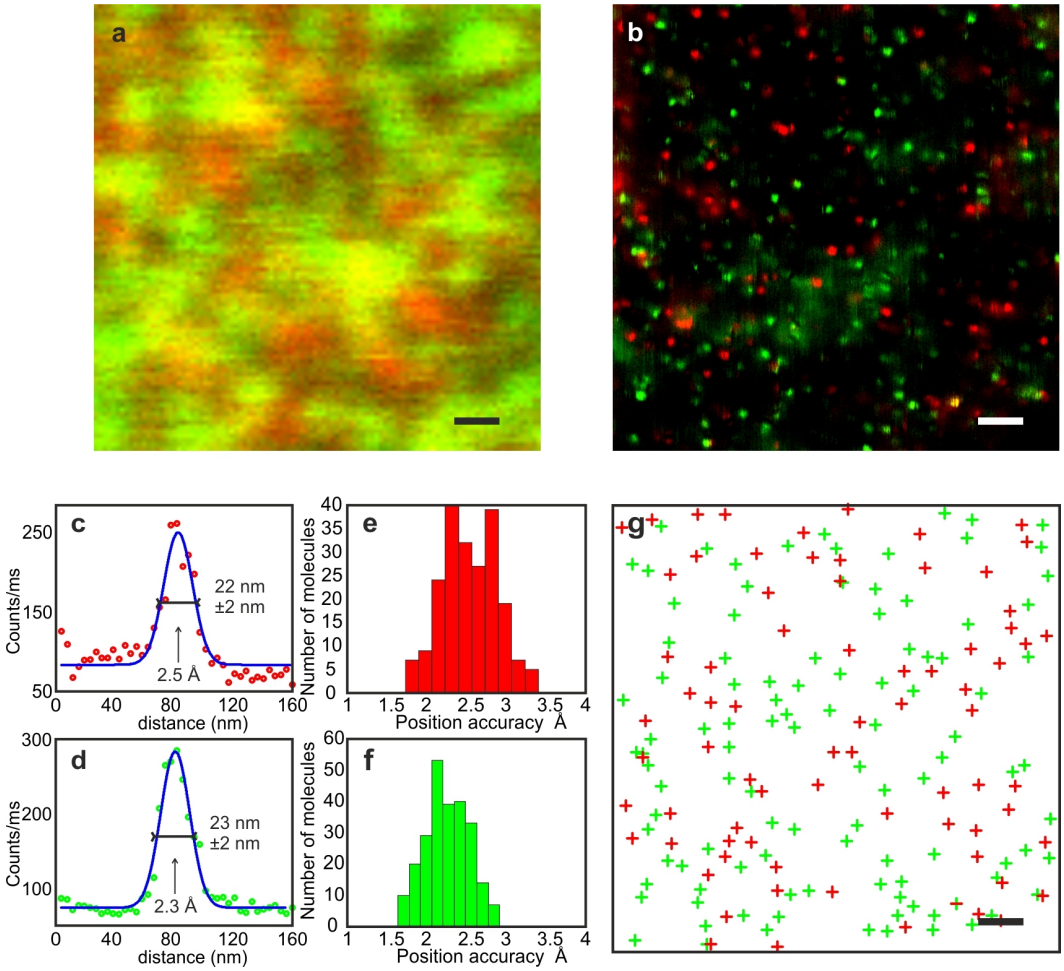

Figure 4.4. *Single molecule optical resolution and localization accuracy with hybrid nano-antenna probes. (a) Dual color confocal image of a sample containing a mixture of DiD and DiI molecules (10^{-6}M concentrations) embedded in a thin polymer layer. The color coding corresponds to the spectral emission of the molecules, green for DiI (excited at λ=560 nm) and red for DiD (excited at λ=633 nm). The yellow color results from the overlap between green and red diffraction limited spots. Scale bar: 200 nm. (b) Dual color near-field image of the same sample obtained with a hybrid nano-antenna having a tip diameter of 25 nm and length of 80nm, excited simultaneously with two laser beams at λ=560 nm and λ=633 nm, under transversal polarization excitation. Scan step size: 3.9 nm, dwell time: 2.5 ms. Scale bar: 200 nm. Comparing (a) and (b) underscores the dramatic increase on resolution and direct capability of spatially distinguishing spectrally different molecules. (c,d) Line profiles over two different molecules, DiD (c) and DiI (d) yielding optical resolutions of ~20 nm for both wavelengths. Resolution is estimated from the FWHM of a Gaussian fitting to the intensity signals. (e,f) Localization accuracies obtained over hundreds of DiD (e) and DiI (f) molecules (having a well-defined circular pattern) from multiple near-field images. (g) The coordinate of each fluorescent spot is calculated with 2Å precision and color-coded plotted according to the emission wavelength. Scale bar: 200 nm.*

4.3. Resolving closely spaced fluorescent molecules

Finally, we took advantage of the dual-color nano-antenna excitation and two-channel detection scheme to resolve closely spaced fluorescent molecules of different spectral characteristics. Figure 4.5a shows examples of proximal DiD and DiI molecules and their respective xy-coordinates (Figure 4.5b). With the narrow intensity profiles and number of photoncounts/spot we directly resolve individual molecules being as close as 2.1 nm (Figure 4.5c). Importantly, the distances between spectrally separated molecules are directly measured with 3 Å accuracy, opening the possibility of addressing multi-molecular complexes at the molecular scale.

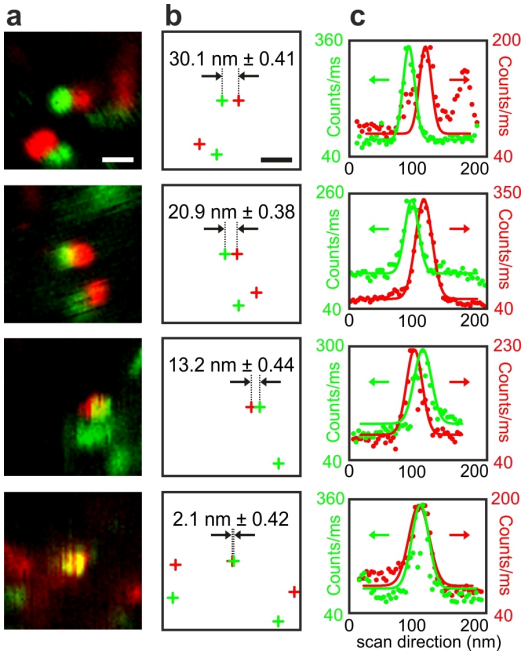

Figure 4.5. *Distance measurements of close-by molecules using dual-color hybrid nano-antennas. (a) Examples of proximal DiD (green) and DiI (red) molecules as extracted from dual color images similar to those shown in Figure 4.4b. Scale bar: 50 nm. (b) Molecular coordinates together with the measured distances between adjacent molecules as determined from the fitting of their intensity profiles as shown in (c).*

Compared to far-field super-resolution methods our hybrid nano-antennas resolve and localize individual molecules based on a single, highly-dense image. Moreover, true nanoscale dual-color optical resolution and sub-nanometric accuracy is obtained using standard florescent probes requiring for this only a modest photon budget, i.e., 10^4 photoncounts/molecule, which is 10^2-fold lower than for localization methods[94]. Because our antennas operate with excitation powers compatible with conventional fluorescence imaging, provide multicolor nanofocusing, and can be operated in a dynamic fashion when combined with fluorescence correlation spectroscopy[95], we anticipate a large number of biological

relevant applications, including unravelling multi-molecular complexes at the molecular resolution level.

Papers related to this chapter :

Mivelle, M. *et al*. Hybrid photonic antennas for subnanometer multicolor localization and nanoimaging of single molecules. *Nano. Lett.* **14**, 4895-4900 (2014).

Mivelle, M. *et al*. Ultrabright Bowtie Nanoaperture Antenna Probes Studied by Single Molecule Fluorescence. *Nano. Lett.* **12**, 5972-5978 (2012).

Chapter 5

Photonic antennas to manipulate the non-radiative energy transfer between quantum emitters

We saw in the previous chapters how metallic or dielectric nanostructures, also called photonic nano-antennas, can convert propagating electromagnetic waves into localized fields at the nanometre scale, and vice versa[1]. Through plasmonic resonances, metallic nano-antennas enhance and confine electromagnetic waves much below the wavelength of light. This property has been used for many purposes, ranging from super-resolution microscopy[29] or biosensing at high concentrations[10] to detection of dynamic events at the nanometre scale[96], and, in particular, to enhance the fluorescence of single emitters placed in their vicinity by manipulating both excitation and emission processes[1,97]. Indeed, photonic antennas modify the local density of states (LDOS) in their vicinity, which in turn affects the total ($k_{tot} = k_r + k_{nr}$), radiative (k_r) and non radiative (k_{nr}) decay rates of nearby quantum emitters[98]. This has the effect of reducing the fluorescence lifetime τ of the emitters ($\tau = \left(k_r + k_{nr}\right)^{-1}$), and modifying their quantum yield ϕ ($\phi = k_r / \left(k_r + k_{nr}\right)$). Interestingly, the latter can either be decreased or increased by the presence of the antenna, depending on the intrinsic quantum yield of the emitter and the competition between k_r and k_{nr} that the antenna generates[99]. Moreover, the fluorescence intensity I emitted by a single emitter is given by $I = k_{exc} \cdot \phi$, where k_{exc} is the excitation rate given by the incident field. Thus, the emitted fluorescence can be also enhanced by the photonic antenna, if the quantum yield and/or the excitation field are increased by the nanostructure[5].

Over the past decade, all of these properties have triggered the application of photonic antennas towards the manipulation of single molecule fluorescence emission demonstrating detection of single molecules at ultra-high concentrations[10], fluorescence enhancement[100] or, like we just saw in the previous chapter, super-resolution imaging[90]. More recently, the process of Förster Resonance Energy Transfer (FRET)[101,102] has been also explored in the context of nano-antennas. FRET is based on the near-field energy transfer between two emitters, from an excited donor to a ground state acceptor. The FRET efficiency, E_{FRET} i.e., the probability that the acceptor will receive the energy once the donor is excited is given by[103]:

$$E_{FRET} = \frac{k_{FRET}}{k_{FRET} + k_d} = \frac{1}{1 + \left(\frac{R}{R_0}\right)^6}$$

where k_{FRET} corresponds to the FRET decay rate constant, and k_d is the donor decay rate (where $k_d = \frac{1}{\tau_d}$; τ_d being the donor lifetime[103]). *R* is the distance between donor and acceptor, and R_0 is the so called Förster radius, i.e., the distance at which E_{FRET} is 50%. R_0 depends on the overlap integral of the donor emission with the absorption spectrum of the acceptor and their mutual dipolar orientation κ. Due to the strong distance dependence between donor and acceptor, FRET is used to accurately measure the nanometric distance between two fluorescent emitters (typically in the range of 1–10 nm) and it is widely applied in biology and chemistry[102].

From the excitation point of view, photonic antennas can open new energy transfer routes due to the reshaping of the near-field becoming comparable to the donor-acceptor distance[104], whereas the modification of the LDOS can affect both, the k_{FRET} and the decay rates of both donor and acceptor[105,106]. As a result, the two main parameters used to experimentally characterize FRET: k_{FRET} and E_{FRET}, can be modified by the presence of the antenna[107-110].

Studies on the effect of plasmonic structures on the process of FRET show that they can help overcoming some of the main limitations of conventional FRET: they can extend the range at which energy transfer occurs[105,111,112] and they can mediate the transfer between perpendicularly oriented dipoles[104,113]. Such advantages make plasmon-assisted FRET a promising strategy for bioimaging. One of the already demonstrated applications uses FRET combined with silver nanoparticles to detect protein-specific sialylation on the cell surface by taking advantage of the enhancement of both the FRET fluorescence signal (having thus a higher contrast) and the FRET efficiency[114]. A second application monitors conformational changes of proteins in living cells with higher sensitivity than with conventional methods thanks to the increased sensitivity to detect changes in FRET efficiency provided by gold-coated coverslips[113].

An additional effect of the coupling between photonic antennas and emitters is the modification of the spatial emission and directionality of the fluorescence emission[92,115-117]. When in resonance, the emitter couples to the nano-antenna so that the radiation proceeds from the coupled system, giving rise to changes in the angular emission. Such changes in emission directionality can be tuned by shifting the antenna resonance and/or by modifying the orientation or the position of the emitter with respect to the antenna. This spatial redistribution of the emission also has an impact on FRET as k_{FRET} is proportional to the field emitted by the donor at the acceptor position[118]. Thus, the FRET rate enhancement can be calculated by computing the ratio between the donor emission in presence and absence of the antenna. By performing such calculations for different acceptor positions, a spatial mapping of the FRET rate enhancement can be readily obtained. Using Finite Difference Time Domain (FDTD) simulations to simulate the donor emission, it has been shown that such enhancement is a function of both the position[105] and the orientation[112] of the donor within the antenna field. However, experiments aimed to validate these simulations have

been performed in solution, where there is no control over the position of the emitters with respect to the antenna. This drawback can be partially overcome by making use of DNA origamis to immobilize the FRET pair at designed positions with respect to the antenna[106,117,119]. Yet, only one relative position can be probed at the time.

In this chapter, I describe the use of photonic antennas carved at the apex of near-field scanning optical microscopy (NSOM) to accurately control the 3D position of antennas over individual FRET pairs, with 2 nm lateral resolution. We experimentally demonstrated FRET modulation up to 15% at the single FRET pair level. Such modulation depends on the relative distance between the antenna and the FRET pairs, and on the donor dipole orientation. Our experimental results together with FDTD simulations further revealed the competition between the FRET rate and donor radiative and nonradiative processes as a function of the emitters-antenna distance.

5.1. Photonic antenna - FRET pair coupling

Figure 5.1a describes the principle of the experiments, where a photonic nano-antenna laterally scans individual FRET pairs with nanometric precision. By varying the relative position between the antenna and the pair during scanning, one obtains a super-resolution map of the antenna-to-FRET-pair coupling, and its impact on k_d, k_{FRET} and resulting FRET efficiency. The experiments have been performed using a combined confocal/NSOM setup (Figure 5.1b) presented previously. Excitation of the sample is achieved either in confocal mode (not shown in the Figure), or by coupling the laser light (λ = 561 nm, 100 nW) at the back-end of a near-field probe supporting the antenna at its apex.

Experiments in confocal mode are performed using circularly polarized light while excitation via the antenna is performed by adjusting the incoming polarized light along the gap region for maximum resonance response (see chapter 4). The sample is mounted on a piezo stage that can be scanned in 3D with nanometre accuracy. The fluorescence emitted from the sample is collected through a 1.3NA objective and split into two single-photon counting avalanche photodiodes (SPAPDs) to discriminate the light emitted from the acceptor and donor molecules.

The antenna geometry used in our experiments is the “hybrid” antenna presented in chapter 4 that consists on a bowtie nano-aperture resonator (BNA) that couples the light onto a monopole[90] (Figure 5.1b). The antennas are fabricated at the apex of aluminum coated tapered optical fibers using focussed ion beam (FIB) and mounted on the NSOM head (Figure 5.1b). The FRET sample consists of double-stranded DNA molecules of 51 base pairs total length, labeled with a single Atto550 donor and a single Atto647N as acceptor set at specific positions on the DNA double strand to reach a separation of 10 base pairs. In these conditions, the donor-acceptor distance is estimated to be 3.4nm which is about twice lower than the Förster radius of R_0 = 6.5 nm assuming an average orientational factor κ^2 = 2/3 for this set of fluorescent dyes. The FRET pairs are immobilized in a PMMA layer at low concentrations to allow for single FRET measurements both in confocal and NSOM modes.

Immobilization in the PMMA improves the photophysical stability of the dyes and prevents any possible dragging by the antenna.

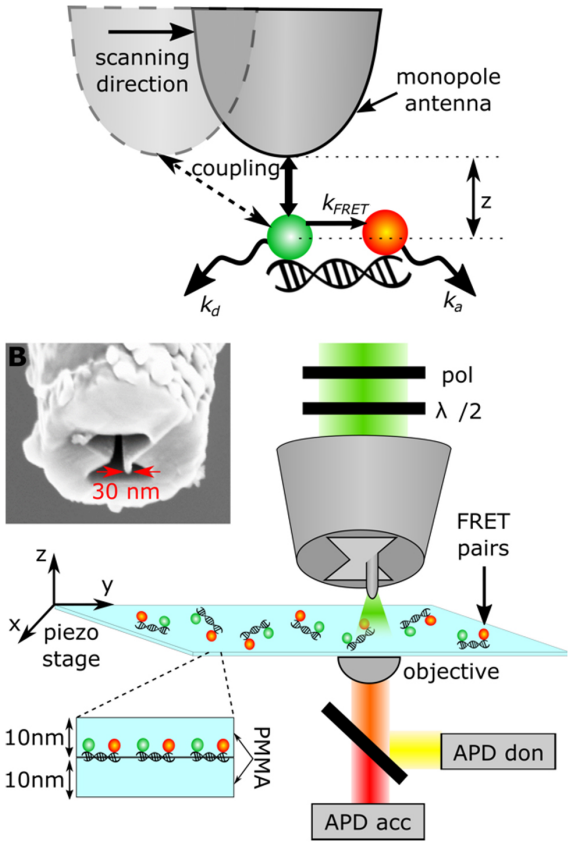

Figure 5.1. *Schematic of an aluminum-based optical antenna probe placed in close proximity to the sample where the FRET pairs are immobilized, and the subsequent detection scheme. The inset shows a SEM image of a representative hybrid antenna probe with a monopole of 30 nm in diameter.*

According to FDTD simulations our hybrid antenna design provides a field enhancement of more than two orders of magnitude (Figure 5.2a) for an incident polarization along the gap and a spatial confinement that matches the diameter of the monopole (30-50 nm)[90]. Due to its geometry, the near-field intensities close to the monopole end exhibit different patterns and degree of enhancement for all 3D orientations (Figure 5.2a), which in turn will affect how dipoles with different orientations are excited. Moreover, we saw in chapter 4 that these types of antennas are broadband over the visible range of the spectrum (Figure 5.2b) significantly overlapping with the absorption and emission spectra of the donor and acceptor dyes used in our experiments (Figure 5.2b).

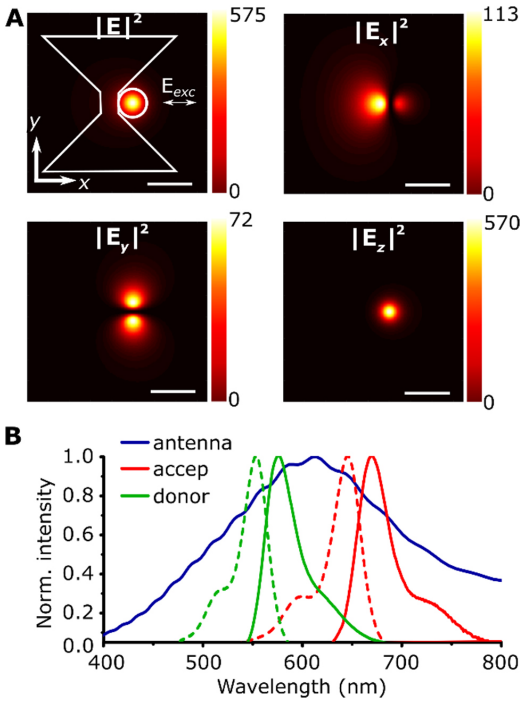

Figure 5.2. *(a) FDTD simulations of the near-field intensity enhancement (ratio of intensity in presence and absence of the antenna) provided by a hybrid antenna (30 nm in diameter, 70 nm in length), 10 nm away from the monopole end. Both the total field as well as the x, y, and z components of the near-field are displayed. Scale bars: 100 nm. (b) Absorption (dashed lines) and emission (solid lines) spectra of both the donor (green) and acceptor (red) dyes. The broad resonance spectrum of the hybrid antenna obtained from FDTD simulations is shown in blue.*5.2.

A representative confocal image of individual FRET pairs is shown in Figure 5.3a. Each spot on the image corresponds to the fluorescence emission of a single FRET pair, where magenta and green represent the acceptor and donor channels respectively. As expected, most of the spots are magenta, consistent with the short distances involved and the estimated E_{FRET} ~ 98%. We attribute the few green spots observed mostly to the fact that the DNA hybridization is not 100% efficient and a non-negligible probability that the two emitters are perpendicular to each other, so that FRET does not occur. Figures 5.3b, c show two exemplary near-field images obtained on smaller regions of the sample using an hybrid nano-antenna. Similar to the confocal case, most of the fluorescence spots are magenta, indicative of high FRET efficiency. In addition, the fluorescence spots show characteristic near-field patterns, i.e., a central bright spot having a full-width-at-half-maximum (FWHM) around 50 nm corresponding to the highly confined excitation from the monopole, together with a weaker shadow region on a side, resulting from residual excitation of the BNA arms. Moreover, based on the FDTD simulations and excitation patterns shown in Figure 5.2, the near-field spots obtained in these images should mainly correspond to out-of-plane oriented molecules, which is expected given the larger field enhancement in the *z* direction (chapter 4).

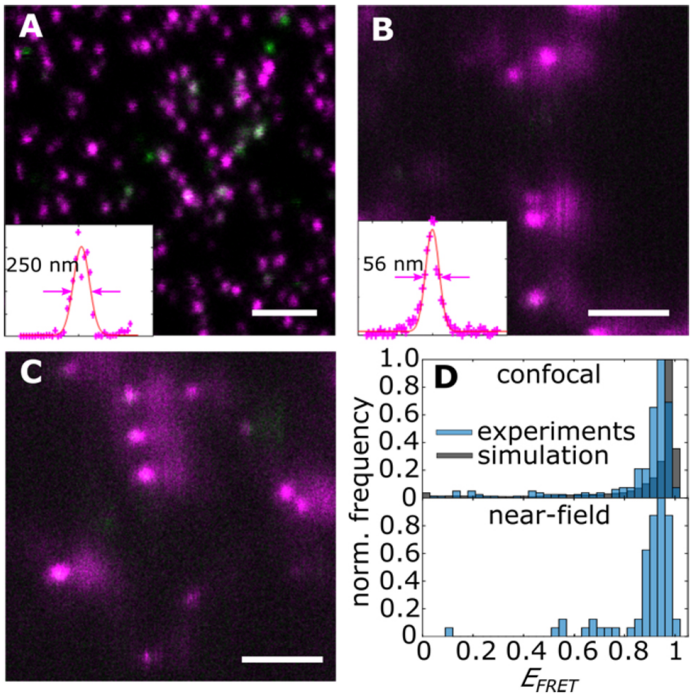

Figure 5.3. *(a) Representative confocal image of a sample containing individual 3.4 nm FRET pairs. Magenta represents signal from the acceptor channel and green from the donor channel. Scale bar: 2 µm. (b, c) Two exemplary antenna-based images of the same sample. Scale bar: 500 nm. Insets in a and b show lines profiles on two different fluorescence spots illustrating the increased lateral resolution obtained by the antenna (b) as compared to diffraction-limited confocal image (a). (d) Upper plot:* E_{FRET} *histogram obtained from the mean intensity of individual spots from multiple confocal images (blue) together with simulated data considering all possible orientations between donors and acceptors (grey). Lower plot: Corresponding* E_{FRET} *histogram obtained from individual spots over multiple antenna-based images.*

The FRET efficiency can be experimentally determined as $E_{FRET} = \frac{n_a}{n_a + n_d}$, where n_a corresponds the number of photons collected in the acceptor channel (after background subtraction), and n_d to the photons collected in the donor channel (background subtracted and after applying a correction factor that accounts for the difference in fluorescence collection efficiencies between both channels). Figure 5.3d shows the histograms of E_{FRET} obtained from the mean intensities of individual spots over multiple confocal images (*upper plot*). The distribution is shifted towards high FRET efficiencies. It is worth noticing that in our case the FRET pairs are immobilized and thus the relative orientation between the acceptor and the donor is fixed, as opposed to most FRET experiments performed in solution where the dyes are freely rotating. In this latter case the orientational factor κ^2 should be considered 2/3, obtained from averaging all orientations, whereas in our case all possible κ

values ranging from 0 to 1 should exist. To assess the effect of κ on the experimentally determined E_{FRET} from confocal images, we generated a histogram from simulated data considering random orientations between the donor and the acceptor. Both experimental and simulated histograms agree nicely with each other validating our experimental approach and detection efficiencies in both channels (Figure 5.3d, *upper plot*).

Figure 5.3d (*lower plot*) shows the E_{FRET} distribution obtained from multiple antenna-based images. For this calculation, we consider the mean intensity of each individual spot, i.e., monopole excitation, disregarding the shadow contribution from the BNA arms. Both confocal and antenna-based E_{FRET} plots are quite similar with a mean E_{FRET} of 0.86 (sd = 0.20) and 0.88 (sd = 0.14) for confocal and antenna excitations respectively. While averaging over all antenna-FRET sample positions and orientations, the initial analysis shows therefore no significant effect of the antenna on the 3.4 nm average FRET efficiency distribution.

5.2. FRET efficiency manipulation

To gain further insight on the potential effect of the antenna position with respect to the FRET pairs, we re-analysed each fluorescence spot and generate E_{FRET} maps on a pixel-to-pixel level. Representative fluorescence and corresponding E_{FRET} maps with a 8 nm pixel resolution are shown in Figures 5.4a, b respectively, together with exemplary zoom-in FRET spots (Figure 5.4c). Interestingly, the FRET efficiency is not homogenous or constant for each single pair, but instead it shows variations up to ~ 20% as a function of the antenna position with respect to individual FRET pairs. Moreover, distinct spatial patterns are observed for different pairs. These effects are more clearly visible when increasing the pixel resolution to 2nm (Figures 5.4d, e) and unequivocally demonstrate nanoscale FRET modulation as the function of the antenna position.

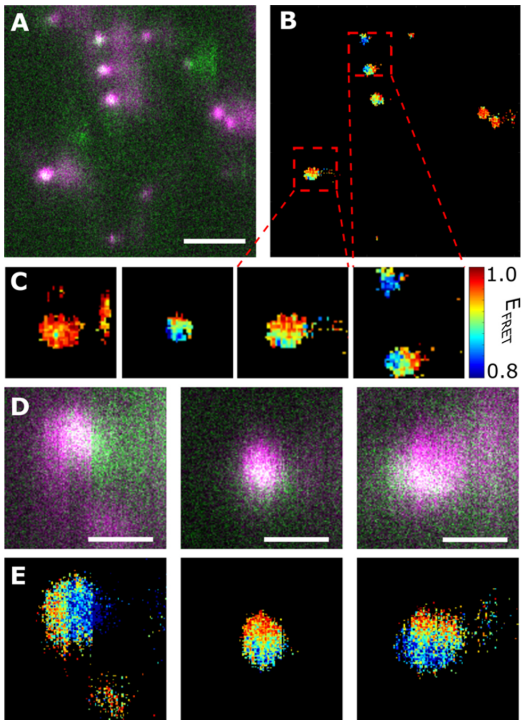

Figure 5.4. *(a) Representative antenna-based image of individual FRET pairs after renormalizing the signal in the donor channel to its maximum. The sample is scanned along the vertical direction. Scale bar: 500 nm. (b) Corresponding* E_{FRET} *map calculated on a pixel-by-pixel basis after applying a 2x2 pixel gaussian filter to the original image for better visualization. (c) Zoom-ins of different* E_{FRET} *spots with a pixel resolution of 8 nm. Each spot shows a different spatial* E_{FRET} *pattern and pixel-to-pixel variations of* E_{FRET} *are readily observed. (d, e) Individual intensity and* E_{FRET} *spots respectively, mapped with a pixel resolution of 2nm. Notice that on the left panel photobleaching of the acceptor occurs during scanning so that the donor signal (green) is recovered and FRET is lost, further demonstrating that our measurements are performed at the single FRET level. Scale bars: 200 nm. Integration time: 10 ms per pixel.*

To quantify better these FRET variations, we generate normalized donor and acceptor fluorescence line profiles on several FRET spots, obtained with a pixel resolution of 8 nm (Figure 5.5). To exclude the influence of residual excitation from the BNA arms, the line profiles are generated vertically along the *y*-scanning direction, and averaged over two line profiles to reduce the effect of photon fluctuations. We assign the zero position in the *x*-axis to the pixel where donor signal is maximal. We further calculate E_{FRET} on every pixel as a function of the antenna position (black lines in Figure 5.5, and expanded on the upper plots) for those pixels where the signal from either of the two channels is at least 20% of its maximum. As observed from the different pairs, the FRET efficiency is not constant but it rather shows variations as a function of the lateral distance between the antenna and the FRET pair. The degree of FRET modulation ranges from 3% up to 15%, depending on the FRET pair. Furthermore, each FRET profile exhibits a different pattern: in some cases, the largest FRET reduction occurs close to centre (i.e., $x = 0$), while in other cases, a gradient

from lower to higher FRET values is obtained. This effect is observed on those pairs where the spots in acceptor and green channels are laterally displaced with respect to each other, and indicate a different coupling of the antenna to the donor and acceptor emitters which in turn depend on the dipole orientation of the emitters with respect to the antenna. Overall, these results show nanoscale FRET modulation mapped with a spatial resolution of ~8 nm and at the single FRET pair level.

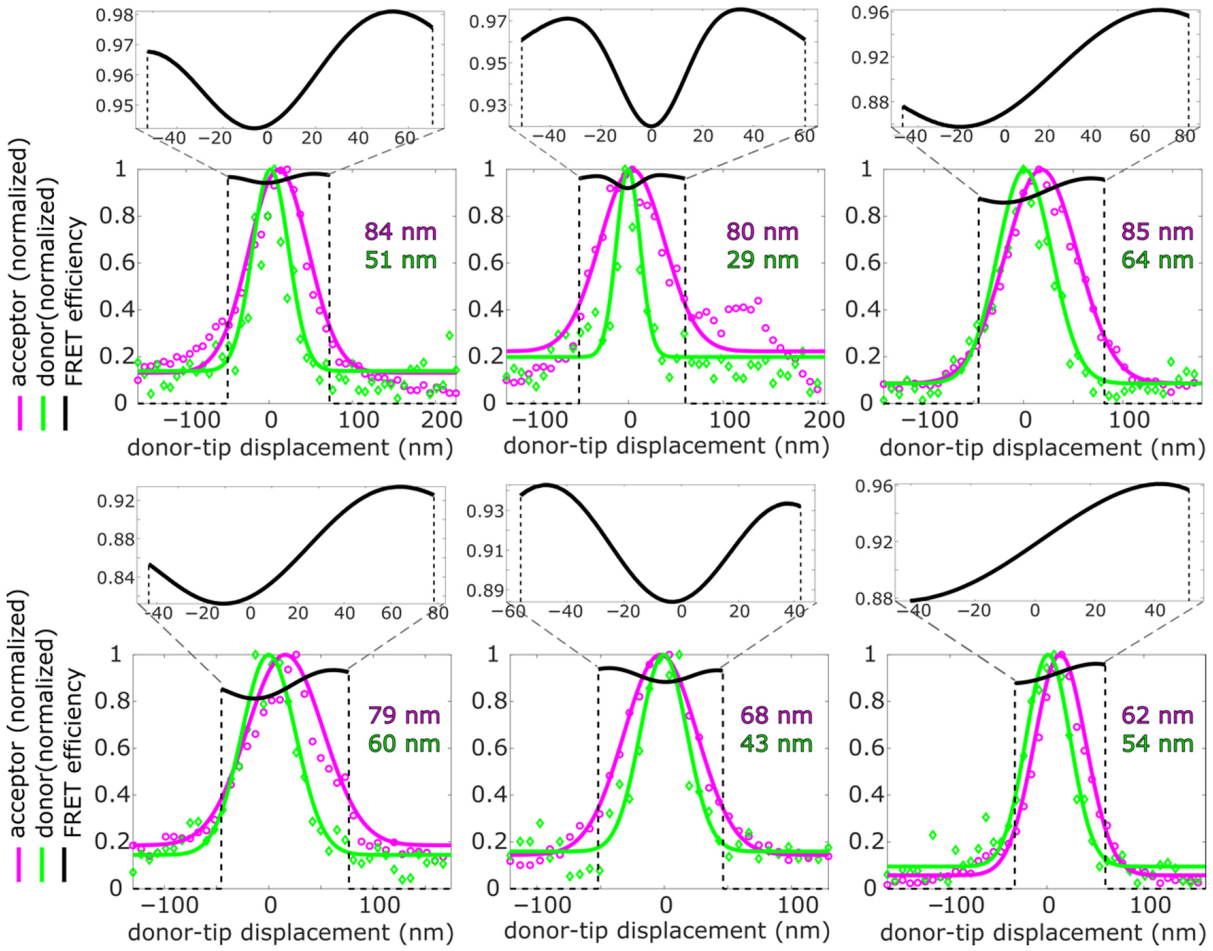

Figure 5.5. *Line profiles of several FRET spots as a function of the antenna position taken along the y-scanning direction. Magenta represents the normalized signal from the acceptor channel, green from the donor channel and black corresponds to the FRET efficiency. Top insets are expanded plots of the FRET efficiency lines profiles. The zero position in the x-axis is defined at the pixel where the donor signal is maximum.*

To understand the influence of the antenna position on the degree of FRET modulation, we performed FDTD simulations. The FRET efficiency is defined as a function of both the FRET and donor rates (k_{FRET}, k_d)

$$E_{FRET}(r) = \frac{k_{FRET}(r)}{k_{FRET}(r) + k_d(r)}$$

By manipulating the equation, we can express it as function of quantities that can be readily simulated:

$$E_{FRET}(r) = \frac{\frac{k_{FRET}(r)}{k^0_{FRET}(r)}}{\frac{k_{FRET}(r)}{k^0_{FRET}(r)} + \frac{k_d(r)}{k^0_{FRET}(r)}} = \frac{\frac{k_{FRET}(r)}{k^0_{FRET}(r)}}{\frac{k_{FRET}(r)}{k^0_{FRET}(r)} + \frac{k_d(r)}{k^0_d(r)}\frac{k^0_d(r)}{k^0_{FRET}(r)}}$$

where $\frac{k_{FRET}(r)}{k^0_{FRET}(r)}$ is the FRET rate enhancement, that can be computed as the ratio of the field emitted by the donor at the acceptor position in presence and absence of the antenna[113], and $\frac{k_d(r)}{k^0_d(r)}$ is the change in donor rates in presence and absence of the antenna. Finally, $\frac{k^0_d(r)}{k^0_{FRET}(r)}$ can be retrieved from the value of the FRET efficiency in a homogeneous environment:

$$E^0_{FRET}(r) = \frac{k^0_{FRET}(r)}{k^0_{FRET}(r) + k^0_d(r)} = \frac{1}{1 + \frac{k^0_d(r)}{k^0_{FRET}(r)}} = \frac{1}{1 + \left(\frac{R}{R_0}\right)^6} \rightarrow \frac{k^0_d(r)}{k^0_{FRET}(r)} = \left(\frac{R}{R_0}\right)^6$$

Therefore, the resultant FRET efficiency at each position of the antenna is the result of a competition between the FRET rate enhancement and the donor rate enhancement[120,121]. Overall, the condition for enhancement of the FRET efficiency[121] requires that $\frac{k_{FRET}(r)}{k^0_{FRET}(r)} > \frac{k_d(r)}{k^0_d(r)}$. Since both parameters depend on the relative position of the donor with respect to the antenna, we expect a modulation of the FRET efficiency while scanning the antenna over the FRET pairs.

Figure 5.6 shows the results of the FDTD simulations, considering two different axial distances from the antenna to the FRET pairs, i.e., *z* = 10 nm (Figure 5.6a) and *z* = 30 nm (Figure 5.6b). Simulations are performed for all three possible orientations of both the donor and acceptor, and for an antenna that scans the donor in the *y* direction, similar to our experimental settings. Moreover, we particularly focus on the influence of the antenna on the donor field as it is the one mostly affecting the acceptor.

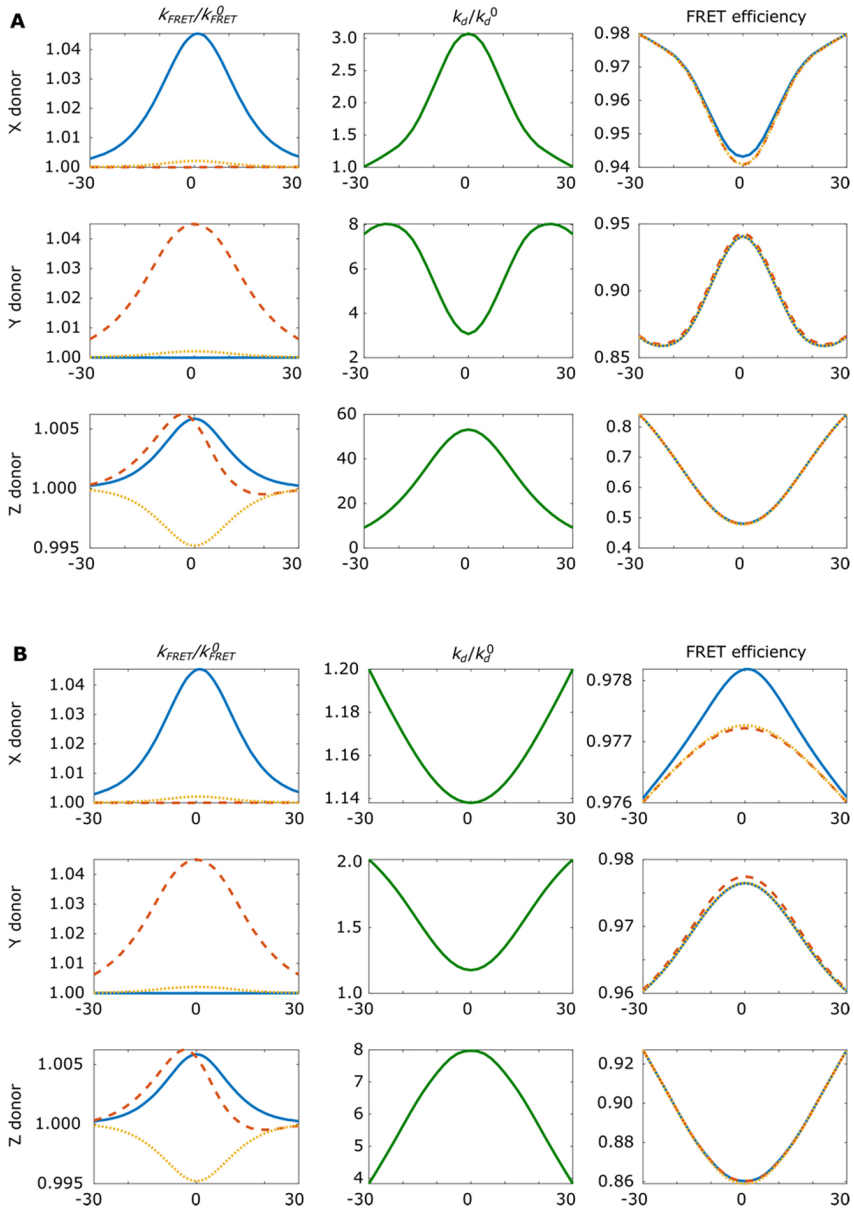

Figure 5.6. *(a, b) FDTD simulations of FRET rate enhancement (left column), donor rate enhancement (middle column) and resultant FRET efficiency (right column) as a function of the lateral antenna position with respect to the donor. The x-axes on the plots correspond to the lateral distance of the antenna with respect to the donor, i.e., as the antenna scans the donor in the y direction (perpendicular to the BNA gap) in analogy to the experimentally obtained line profiles. x = 0 corresponds to the position where the antenna is vertically aligned with the donor. Simulations are shown for different dipolar orientations of the donor (x in first row, y in the second and z in the third row) and consider the 3D near-field components emitted by the donor (in the x-direction: solid blue, in the y-direction: dashed red and in the z-direction: dotted yellow). In the case of the donor rate enhancement, only the donor orientation plays a role (shown as green lines). The simulations are shown for an axial separation between the donor and the monopole end of (a) 10 nm and (b) 30 nm.*

As observed from the simulations considering FRET pairs with a short separation of 3.4nm between donor and acceptor emitters, the donor rate enhancement $\frac{k_d(r)}{k_d^0(r)}$, is always much higher than the FRET rate enhancement $\frac{k_{FRET}(r)}{k_{FRET}^0(r)}$, for any donor orientation. Therefore, under our experimental conditions, variations on the FRET efficiency was dominated by the donor rate enhancement. Furthermore, since $\frac{k_d(r)}{k_d^0(r)}$ is independent on the acceptor orientation, the FRET efficiency modulation by the antenna only depends on the donor position, as shown on the most right column of Figure 5.6. Moreover, the strength of the FRET efficiency modulation depends on the dipolar orientation of the donor, being more pronounced for *z*-oriented donors as they couple more efficiently with the antenna (third row on Figures 5.6a, b). Since the near-field excitation provided by the antenna is stronger in the *z* direction (Figure 5.2), donors aligned along the *z* direction will be most efficiently excited and FRET will largely proceed from these pairs. In these conditions, we expect from our simulations to preferentially measure a FRET efficiency reduction, which is fully consistent with our experimental results. Finally, the strength of FRET modulation strongly depends on the axial distance separation between the antenna and the donor emitter (simulations at *z* = 10 nm in Figure 5.6a and *z* = 30nm for Figure 5.6b). At *z* = 10nm the drop in FRET efficiency caused by the donor enhancement rate is 40% and decreases to ~10% for an axial separation of 30 nm. Bearing in mind our sample preparation procedure where the FRET pairs are buried within a thin PMMA layer, our experimentally obtained FRET modulation values of 3-13% agree well with an axial distance separation between the antenna and the donor ~30 nm.

5.3. FRET rate vs Decay rate : the key element

Interestingly, the experimental data shown in Figure 5.5 also shows a consistent narrower profile of the donor signal as compared to the acceptor one. To enquire whether this observation is statistically significantly, we analysed over 30 different FRET spots and measured their FWHM (Figure 5.7a). The histogram shows a clear narrowing of the donor profile as compared to the acceptor. To exclude any potential artefacts induced by the antenna and/or the experimental set-up we performed similar measurements on 20nm-beads deposited on glass coverslips (Figure 5.7b). As expected, the distributions for both channels fully overlap with each other, rendering an effective confinement of ~ 60nm, and demonstrating that the narrowing of the donor profile exclusively occur as a result of FRET and donor coupling to the antenna. These results can be understood on the basis that E_{FRET} results from a competition between k_d and k_{FRET} (Figure 5.7c). Based on our simulations (Figure 5.6), at lateral positions away from the antenna, k_{FRET} dominates and the donor signal is highly quenched. However, at lateral positions close to the antenna (within ~ ± 15nm as inferred from Figure 5.6), the donor rate enhancement is highly increased and

competes with k_{FRET}, leading to donor emission. Our experimental data agrees remarkably well with the simulations, as the donor FWHM profile ~ 30 nm narrower than the acceptor emission profile. It worth noticing that the acceptor FWHM profile is somewhat broader than that obtained on the calibration beads. This difference essentially stems from the fact that the acceptor emitter is located at a longer axial distance with respect to the antenna since it is buried in the PMMA layer, as compared to the beads which are deposited directly on glass coverslips. In summary, by laterally manipulating with nanometric precision the 3D position of the antenna with respect to the emitters, we are able to directly map the competition between k_d and k_{FRET} and experimentally measure FRET modulation induced by photonic antennas.

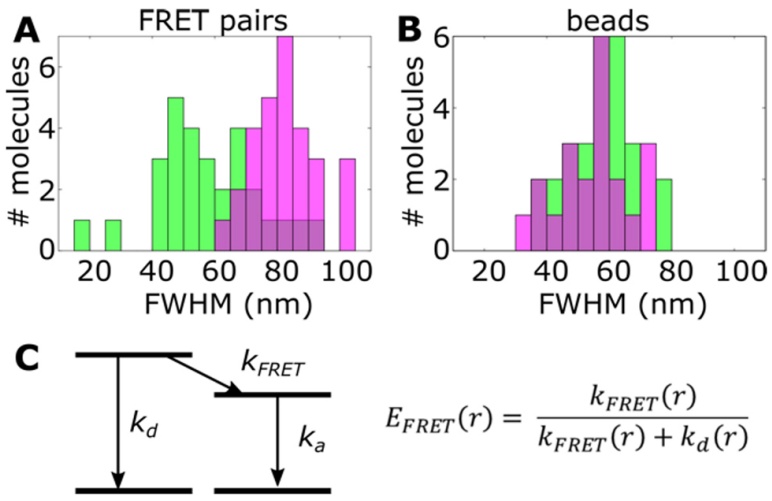

Figure 5.7. *(a) Histogram of the FWHM obtained from different FRET pairs, where green and magenta correspond to donor and acceptor emitters, respectively. (b) Corresponding histogram obtained on 20-nm beads measured using the same antenna and under similar experimental conditions. (c) Schematics of the FRET process, where k_a (acceptor emission rate) depends on the competition between k_d and k_{FRET}.*

In conclusion, we have used our hybrid nano-antennas mounted on a near-field optical set-up to achieve full 3D control of the antenna position with respect to single FRET pairs. Using this approach we have directly mapped the FRET efficiency as a function of the antenna-pair distance, with a lateral precision of 2 nm. Our experiments have shown that the resulting energy transfer depends on the position of the antenna with respect to the pair and on the donor dipole orientation. For a system with high FRET efficiency such as the one studied here (3.4 nm separation), the donor enhancement rate dominates over the FRET rate resulting in an overall decrease of FRET efficiency between 3-15%. This work constituted the first experimental visualization of how photonic antennas influence the competition between k_d and k_{FRET}, controlling the FRET efficiency. I think it would be now interesting to

study in the future similar effects on FRET pairs of larger separations. Such experiments will be interesting given the broad applicability of FRET and the prospect that photonic antennas can extend the range at which FRET can be observed.

Paper related to this chapter :

Sanz-Paz, M. *et al*. Nanoscale control of single molecule Förster resonance energy transfer by a scanning photonic nanoantenna. *Nanophotonics* **1** (2020).

Mivelle, M. *et al*. Hybrid photonic antennas for subnanometer multicolor localization and nanoimaging of single molecules. *Nano. Lett.* **14**, 4895-4900 (2014).

Mivelle, M. *et al*. Ultrabright Bowtie Nanoaperture Antenna Probes Studied by Single Molecule Fluorescence. *Nano. Lett.* **12**, 5972-5978 (2012).

Part 3. Coupling of magnetic light and matter through photonic antennas

In this last part, we will see that the local density of optical states ("LDOS") is multiple and vectorial, and its manipulation is not the prerogative of electrical nano-antennas. Indeed, when we talk about LDOS, it is often implicitly considered as electrical. However, an LDOS can be electric or magnetic. In the first chapter (chapter 6), we will see theoretically that a magnetic emitter's total decay rate can be strongly increased when it is put in contact with an optical nano-antenna designed to increase the magnetic LDOS in the near field strongly. This chapter reflects the exact moment in my young career when I started to conceive a research project of my own. It is indeed at this moment that I decided to orient myself towards the study of the coupling between magnetic light and matter. It is from these ideas and this study, which I carried out when I was still a post-doc at ICFO, that I built my CNRS research project on which I was recruited.

Finally, in the last chapter of this manuscript (chapter 7), we will see experimentally that a dielectric nano-antenna also designed to modify the magnetic LDOS allows to manipulate the luminescence emission of a nanocrystal doped with trivalent europium ions, known to possess purely magnetic transitions. This last chapter is on one side the achievement of my training as a researcher, but as well the beginning of my life as a researcher. Indeed, this work is directly linked to my CNRS research project but it is also the result of ideas that started during my thesis. It is also the first project that I led as a permanent researcher, project that involved two PhD student, Cyrine Ernandes and Maria Sanz.

Based on this study and by relying on solidly established collaborations, a Parisian and academic environment rich in interactions and possibilities, experimental, theoretical, human and financial resources, I can now project myself with serenity into the future on new research topics.

Chapter 6

Photonic antennas to enhance the magnetic local density of states

The interaction between light and matter is widely considered being solely mediated by the electric field. This assertion also applies in the Bohr model, which holds that magnetic dipole transitions are about 10^5 times weaker than electric dipole transitions[39], and are therefore considered marginal. In this context, many researchers have aimed to control the spontaneous emission of electric dipole transitions through devices such as microcavities[122], photonic crystals[123] or optical antennas[98,124]. All of these approaches rely on the modification of the electric local density of states (ELDOS) in the vicinity of the considered electric dipole, characterized through the Purcell effect. Nowadays, this effect is commonly used to quantify the total decay rate enhancement of such electric dipole transition, but it was originally employed to describe nuclear magnetic resonance decays[125].

In parallel, it is also known that complex molecules have magnetic dipole moments in the optical domain. However, these optical transitions are extremely weak compared to their electric dipole transitions (about 10^2 to 10^5 times weaker[39,126]). In order to amplify the absorption and/or emission of these transitions it is thus interesting to enhance the optical magnetic field together with the magnetic local density of states (MLDOS) around the molecules.

Recently, researchers have demonstrated that magnetic dipole transitions could also be studied in materials such as lanthanide[127,128] and generally in metallic[129] ions. In these studies, it was shown that the MLDOS could be engineered in the same way as its electric counterpart[130,131]. In particular, the oscillating behavior of the MLDOS in space could be recorded in close proximity to metallic surfaces[132] in good agreement with theoretical predictions. Nevertheless, only non-resonant structures were experimentally used at that time to study the MLDOS sensed by magnetic transitions.

I have described in the first part of this manuscript how nanophotonic and plasmonic structures could modify the behavior of electric[1,3,90] and magnetic[36,37,46,133] fields in the near field, making these nanostructures ideal candidates to strongly enhance the magnetic field of light[33]. These nanostructures could then actively control magnetic dipole transitions in matter. Indeed, it has been demonstrated theoretically that nanostructured dielectric[8] and metallic[50] materials could be used to modify locally the MLDOS. We therefore expected that tailored resonant plasmonic nano-antennas could be applied to significantly change the MLDOS near magnetic dipole transitions, leading to an increase of the magnetic emission of the material carrying these transitions.

In this chapter, I will theoretically describe how to achieve a strong enhancement of both the total and radiative decay rates of a magnetic dipole moment by using the resonant nano-

antenna presented in chapter 2 and designed to strongly enhance the optical magnetic field of light in the near-field at the telecom wavelength (λ=1550 nm)[51]. I will also show that these strong enhancements are magnetic dipole specific and are not related to an increase, in the same proportion, of the total and radiative decay rate of an electric dipole moment. Furthermore, I'll compare the effect on the quantum yield of the magnetic dipole moment of an optical nano-antenna alone as opposed to the so-called "sandwich" optical nano-antenna configuration, also known as Metal-insulator-Metal (MIM) nano-antenna configuration. Finally, I'll theoretically describe and quantify the modification of the MLDOS in the near field of a resonant optical nano-antenna by mapping the total decay rate in a plane situated in close proximity to the nano-antenna. Importantly, in the same way than the electric antennas presented in part 2, I'll demonstrate that resonant plasmonic nano-antennas are unique to strongly modify the emission of a magnetic nanosource at the nanometer scale, opening up new exciting possibilities in magneto-optics.

6.1. Diabolo antennas to manipulate magnetic fields

We used finite difference time domain (FDTD) simulations to calculate the optical magnetic response of two different optical nano-antennas, a diabolo nano-antenna[33] (described in chapter 2) and a sandwich diabolo nano-antenna (two diabolo nano-antenna superposed and separated by an insulator). The optical nano-antennas are chosen to be in aluminum with a dielectric constant given by a Drude model at λ = 1550 nm, and are surrounded by air (optical index of 1). The excitation of the antennas is made by two different sources, depending of the type of studies: a plane wave or a magnetic dipole moment, as described later in this chapter.

The total (Γ_{tot}) and radiative (Γ_{rad}) decay rate enhancement of the magnetic emitters placed in the vicinity of the optical nano-antennas are calculated and described by the equations:

$$\Gamma_{tot} = \frac{P_{tot}}{P_0} \qquad (1)$$

and

$$\Gamma_{rad} = \frac{P_{rad}}{P_0} \qquad (2)$$

where P_{tot} and P_0 are the total powers emitted by the magnetic dipole with and without the optical nanostructures, respectively. P_{rad} is the power radiated in far-field in presence of the optical antennas. These values are calculated at each position of the dipole with respect to the nano-antennas. For all the calculations, we consider that the magnetic dipoles have an intrinsic quantum yield of 1.

The quantum yield (η) of the magnetic nanosource is then obtained through the equation:

$$\eta = \frac{\Gamma_{rad}}{\Gamma_{tot}} \qquad (3)$$

We have explored two different nano-antenna configurations, 1) a single diabolo nano-antenna[33] (Figure 6.1a), consisting of two metallic triangles separated by a metallic junction, and 2) the sandwich diabolo (S-diabolo) nano-antenna, made of two identical diabolos separated by an air gap of nanometric size (Figure 6.1b). The dimensions of these two configurations have been chosen such that the nanostructures generate a single magnetic hot spot at the metallic junction and at the telecom wavelength (λ=1550 nm). The excitation is made with a plane wave launched 1 µm below the nanostructures, linearly polarized along the *y*-axis and propagating along the *z*-axis, as shown in Figures 6.1a and b. Figures 6.1c and d show the spectral responses of the diabolo and S-diabolo, respectively, calculated at a point centered on their metallic junction, 10 nm away from the metal. In this plane and at this position, the magnetic field is the strongest due to an intense electrical current flowing through the metallic junction under certain excitation conditions, as explained in chapter 2. As clearly seen, both configurations enhance the magnetic field by more than two orders of magnitude (Figures 6.1c, d). Furthermore, the spectral response is broader for the diabolo antenna (Figure 6.1c) compared to the S-diabolo (Figure 6.1d), with quality factors of 4.18 and 7.28 respectively at their resonances. These results indicate that the energy is stored more efficiently in the case of the MIM configuration and dissipated faster, mainly through radiative channels, in the case of the diabolo.

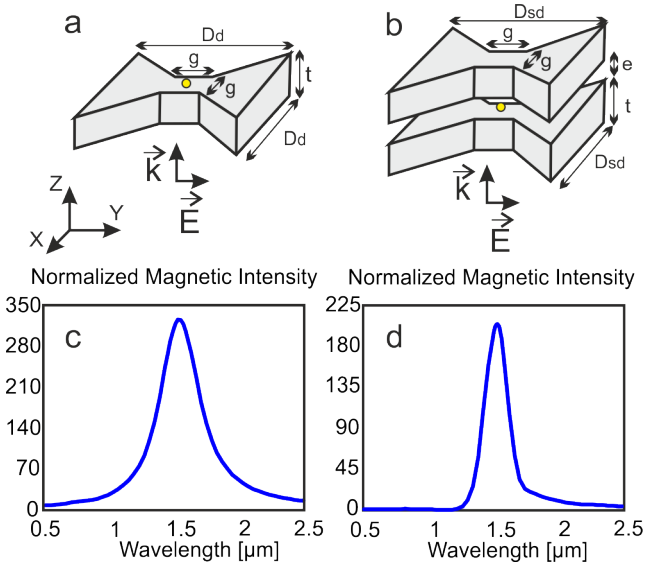

Figure 6.1. *Antenna spectral responses. (a, b) 3D schematics of the diabolo (a) and S-diabolo (b) antennas, with t=55 nm, g = 50 nm, e=15 nm, D_d=335 nm and D_{sd}=240 nm. The yellow point corresponds to the position where the spectra are calculated, 10 nm away from the antennas and centered on the metallic junctions. (c, d) Spectral magnetic intensity responses of the diabolo (c) and the S-diabolo (d). The vectors **k** and **E** represent the direction of propagation and the polarization of the electric field respectively.*

In order to compare the two configurations in terms of field enhancement and confinement we calculated the normalized magnetic and electric field intensity distributions (H_{tot}^2/H_0^2 and

E_{tot}^2/E_0^2 respectively) in the (*xy*)-transversal and (*xz*)-longitudinal planes for each antenna under similar excitation conditions as used for Figures 6.1a, b. H_{tot}^2, E_{tot}^2 and H_0^2, E_0^2 represent the magnetic and electric field intensity with and without the antenna, respectively. In agreement with our previous reports[33], we find that the magnetic field in the case of the diabolo antenna is localized around the metallic junction between the two metallic triangles (Figures 6.2a, e), whereas for the S-diabolo, the field is confined between the two metallic junctions of the two diabolos (Figures 6.2c, g). On the other hand, the electric field distribution for both structures is strongly delocalized towards the extreme parts of the antennas (Figures 6.2b, f for the diabolo and 6.2d, h for the S-diabolo) and do not overlap with the magnetic field distribution. Furthermore, the electric intensity is not confined into a small area, as its magnetic counterpart, although it still shows a certain degree of enhancement particularly in the *(xy)*-plane (Figure 6.2b), directly related to the magnetic field enhancement, as previously reported[33]. In the *(xz)*-plane, both the diabolo and S-diabolo configurations provide between one to two orders of magnitude higher enhancement of the magnetic field (Figures 6.2e, g) compared to the electric field (Figures 6.2f, h), underscoring the potential of these nanostructures to selectively magnify and confine magnetic fields.

Interestingly, the magnetic field intensity in the (*xy*)-transversal plane is higher and more confined in the case of the S-diabolo than in the diabolo (Figures 6.2a, c). Moreover, in the (*xz*)-longitudinal plane, the maximum of magnetic field intensity for the diabolo is slightly higher than for the S-diabolo (Figures 6.2e, g). This behavior is in apparent contradiction with studies reporting that sandwich structures are better suited for enhancing magnetic fields[134,135]. This effect can be understood by the fact that the diabolo is already a very efficient system to enhance the magnetic field and that coupling two diabolo antennas in air lowers the enhancement due to a screening effect of one of the diabolos with respect to the other. Notably, the magnetic field for the S-diabolo is significantly more confined than for the diabolo, with a mode volume of the electromagnetic energy density of about $(\lambda/16)^3$ nm^3 in the case of the diabolo and $(\lambda/30)^3$ nm^3 in the case of the S-diabolo. This higher degree of confinement is a direct effect of the coupling between the two diabolos nano-antennas.

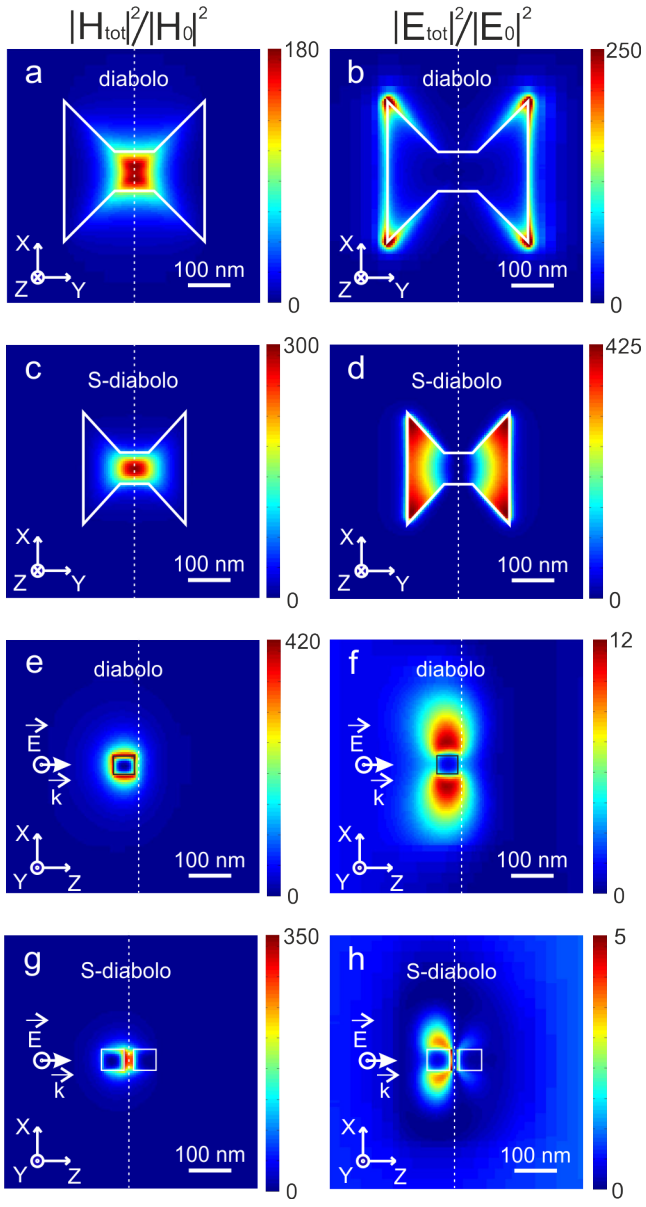

Figure 6.2. *Normalized (a, c, e, g) magnetic and (b, d, f, h) electric intensity distributions in the case of (a, b, e, f) the diabolo and (c, d, g, h) the S-diabolo nano-antennas. The distributions are plotted in a xy-transversal plane, 10 nm away from the antennas (a-d), and in a xz-longitudinal plane (e-h), through the center of the metallic junction. The dashed lines in (a-d) represent the transversal planes shown in (e-h) and vice versa. The vectors* ***k*** *and* ***E*** *represent respectively the direction of propagation and the polarization of the electric field launched in the simulation. The solid lines surrounding the antennas are guides to the eyes.*

Given the large enhancement of the magnetic field and its spatial delocalization with respect to the electric field, these plasmonic nanostructures should be well suited to locally control magnetic transitions in matter. To assess this possibility, we studied the effect of these two different nanostructures on the decay rates of point-like optical emitters described by a magnetic and an electric dipole moment. We performed a series of simulations by placing

the dipole in the maximum of the magnetic field of each structure (*i.e.*, near their metallic junctions) and then scanned the dipole along the antennas, as schematically shown in Figures 6.3a and b. In here, we assume that the dipole point source is a good approximation for a magnetic or electric dipole transition, as previously reported in the case of electric dipole transitions[15,115,118] described by electric dipole sources. The simulations consist of scanning the dipole along the three spatial dimensions in the case of the diabolo, and in the transversal plane in the case of the S-diabolo (Figures 6.3a and b). For each position of the dipole with respect to the antennas, Γ_{tot} and Γ_{rad} are then calculated using equations 1 and 2 and following the approach of Kaminski et al[136], adapted for magnetic dipoles[51].

6.2. Strong manipulation of magnetic quantum emitters

We first addressed the influence of the antennas on the magnetic dipole. Due to the resonance properties of the antennas and their magnetic field components along *x, y* and *z* in near field[33], we chose the magnetic dipole moment to emit at a wavelength of 1550 nm and to be oriented along the *x*-axis, which is the orientation of the magnetic field at the center on the antennas, i.e., at the metallic junction[33] (Figures 6.3a and b). Figures 6.3c and d show Γ_{tot} as a function of the dipole position for the diabolo and S-diabolo, respectively, while Figures 6.3e and f show their Γ_{rad} counterpart. The total decay rate of the magnetic dipole is enhanced by respectively two and three orders of magnitude for the diabolo and the S-diabolo when the dipole is centered on the metallic junction. Furthermore, the radiative decay rate is also enhanced by two orders of magnitude for both antennas. This result is extremely important since the radiative decay rate directly determines the amount of photons emitted in the far field by the nanosource.

Moreover, as observed in Figures 6.3c-f, both Γ_{tot} and Γ_{rad} rapidly decay when the dipole moves further away from the metallic junction. This decay is stronger along the *x* and *z* direction than along the *y*-direction, which is explained by the proximity of the metal along *y* continuing to influence those rates at each dipole positions[137].

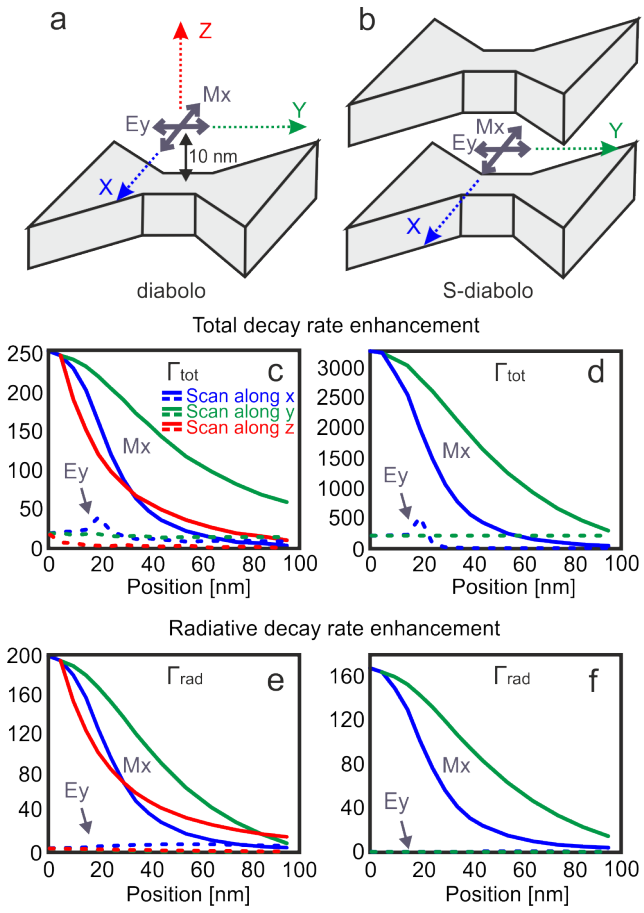

Figure 6.3. *Total and radiative decay rate enhancements of an optical nanosource described by a magnetic or an electric dipole moment. (a, b) 3D schematics of the simulations performed; a magnetic (Mx) or an electric (Ey) dipole moment oriented along x or y respectively is placed in near proximity of the diabolo and S-diabolo metallic junctions (10 nm away) and scanned along (a) the x, y, z directions in the case of the diabolo and (b) x, y directions in the case of the S-diabolo. (c, d) Γ_{tot} and (e, f) Γ_{rad} for each position of these dipoles (continuous lines correspond to the magnetic dipole, dashed lines to the electric dipole) along the diabolo (c, e) and the S-diabolo (d, f).*

To compare the influence of the resonant antennas on the enhancement of the decay rates between magnetic and electric dipoles, we performed similar studies on an electric dipole. For this, a *y*-oriented electric dipole is scanned along the antennas (Figures 6.3a and b) and for each position the values Γ_{tot} and Γ_{rad} are calculated in the same way as for the magnetic dipole presented above. In here, the electric dipole orientation is chosen to be collinear to the polarization of the resonant excitation field (Figure 6.2) and to the electric current (responsible for the magnetic field enhancement) running through the antenna[33].

For both antenna configurations, at the maximum of the magnetic Γ_{tot}, its electric counterpart is more than one order of magnitude lower, confirming that these antennas are better suited to strongly modify the magnetic dipole emission at the nanoscale. Moreover, the ratio between electric and magnetic Γ_{rad} reduces even more due to a strong quenching of the

electric dipole emission; indeed, the electric Γ_{rad} is barely present in the case of the S-diabolo (Figure 6.3f). As mentioned above, these calculations have been made for two specific orientations of the electric and magnetic dipoles. In order to fully cover the coupling between these antennas and such dipoles, we also calculated the averaged enhancements of Γ_{tot} and Γ_{rad} for dipoles oriented along the 3 main directions (*x*, *y*, *z*) and centered 10 nm above the metallic junction. The enhancements of the average magnetic Γ_{tot} and Γ_{rad} are then respectively 106 and 67 in the case of the diabolo and 1155 and 56 in the case of the S-diabolo. In contrast, the enhancements of the average electric Γ_{tot} and Γ_{rad} counterparts are respectively 43 and 1.9 in the case of the diabolo and 221 and 2.63 in the case of the S-diabolo. These results demonstrate once more the ability of diabolo and S-diabolo antennas to strongly influence the total and radiative magnetic dipole emission and their poor performance to modify the radiative electric dipole emission.

Having the total and the radiative decay rates, the quantum yield (η) for each position of the magnetic dipole along the two antennas can be calculated using equation 3. The results are plotted in Figure 6.4. Interestingly, for the diabolo antenna, η becomes very large when the dipole is centered on the antenna, with about 80% of the energy radiated in far field. These results indicate that the diabolo geometry is a very efficient optical antenna when coupled to a magnetic nanosource. Moreover, this value remains rather constant when the dipole moves along the *x* and *z* directions and decays along the *y* direction due to higher absorption into the metal. On the other hand, the large enhancement of the total decay rate in the case of the S-diabolo, is made at the expense of a very low η of about only 5%. This makes in practice this sandwich antenna a very inefficient system to be coupled to a magnetic dipole transition, despite its high radiative decay rate. Therefore, the use of the S-diabolo to strongly reduce the lifetime of magnetic emitters might be appropriate, but in order to enhance the fluorescence of a magnetic emitter, the diabolo configuration alone is preferred.

In addition to these results, it is worth noticing that placing an electric dipole in close proximity to the metallic junction of these two structures, aside from reducing Γ_{tot} and Γ_{rad} by more than one order of magnitude with respect to a magnetic dipole, it also strongly reduces η, with 20 % and less that 0.1 % efficiency for the diabolo and the S-diabolo respectively.

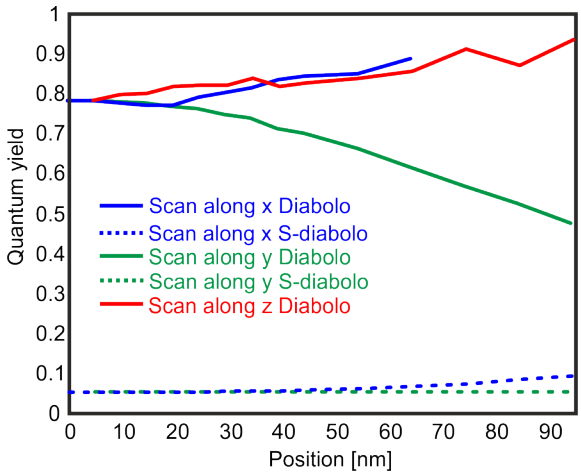

Figure 6.4. *Quantum yield of the magnetic dipole for each spatial position for both the diabolo and the S-diabolo nano-antennas.*

6.3. Magnetic local density of state mapping

Finally, in order to fully describe the coupling between the diabolo nano-antenna and the magnetic dipole, we performed simulations to describe the effect of the diabolo on the MLDOS in a transversal plane 10 nm away from the diabolo (Figure 6.5a). Figure 6.5b displays a three dimensional map of the total decay rate enhancement superimposed to the diabolo nano-antenna which is directly proportional to the MLDOS[7]. Therefore, it can be clearly seen that the MLDOS is strongly affected on a very small area near the metallic junction, corresponding to the region where the magnetic field is also strongly enhanced, as shown in Figure 6.2a and b.

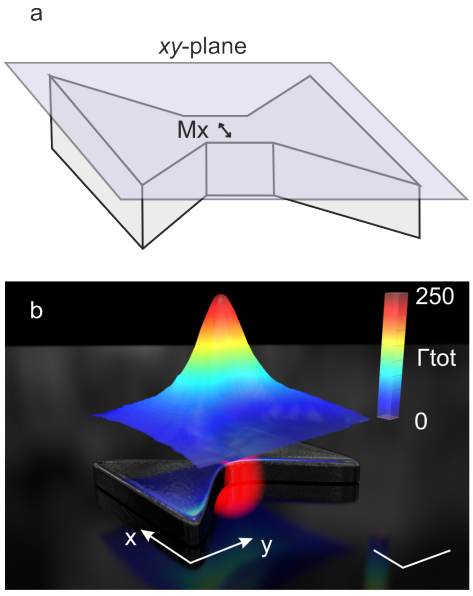

Figure 6.5. *MLDOS mapping. (a) 3D schematic of the simulations performed; a magnetic dipole oriented along x is placed near the diabolo antenna (10 nm) and scanned along a xy-plane. At each position, Γ_{tot} is calculated. (b) 3D plot of the MLDOS superimposed to the diabolo antenna. The scale bars are 100 nm.*

In summary, I have theoretically shown an increase of two to three orders of magnitude on both the total and radiative decay rates of a magnetic dipole moment by placing it in near proximity of a plasmonic nano-antenna designed to create a single magnetic hot spot at the nanometer scale. These strong enhancements have been demonstrated for both diabolo and S-diabolo antennas and are confined in a small subwavelength volume close to their metallic junction. Furthermore, I showed oppose effects of these two antennas on the quantum yield of the magnetic dipole, i.e., the diabolo behaves as an efficient antenna while the S-diabolo quenches the emission. Finally, I presented a theoretical distribution of the MLDOS in the entire plane close to a diabolo optical nano-antenna, providing a thorough understanding of the antenna influence on a magnetic dipole transition.

These results highlight the unique ability of such optical nano-antennas to enhance and control light emission from magnetic dipole transitions in matter, for example in lanthanide ions. In particular, the diabolo nano-antennas would be extremely well suited to study such transitions in Er^{3+}, as this ion is known to sustain a strong magnetic dipole transition[73] at the telecom wavelength and serves as an important emitter in a wide range of technological applications.

Paper related to this chapter :

Mivelle, *et al*. Strong Modification of Magnetic Dipole Emission through Diabolo Nanoantennas. *ACS Photonics* **2**, 1071-1076 (2015).

Grosjean, T. *et al*. Diabolo nanoantenna for enhancing and confining the magnetic optical field. *Nano. Lett.* **11**, 1009-1013 (2011).

Chapter 7

A dielectric antenna to manipulate the quantum magnetic emission

Landau postulated that the oscillation of light in the visible range was too fast to consider the influence of the optical magnetic field on the electrons,[38] justifying the magnetic permeability approximation $\mu(\omega) = \mu_0$ for macroscopic materials. Nevertheless, at the quantum level, the interaction between light and a quantum emitter is represented by a multipolar expansion of the interaction Hamiltonian:[39]

H_{int}= -p·E(t) - m·B(t) - [Q∇]·E(t) - …(1)

where p and m correspond to electric and magnetic dipoles, E and B to the electric and magnetic fields, and Q to the electric quadrupole. As I discussed in chapter 6, if allowed by the selection rules, the term p·E(t) is orders of magnitude higher than any other term of equation 1, and this is why efforts have been made to mostly control, manipulate and enhance the emission of electric dipole sources. This has been achieved by means of interfaces[137], cavities[122], photonic crystals[123], and more recently by using plasmonic [98,124] and dielectric nano-antennas[138-142]. Although the electric interaction is significantly stronger than its magnetic counterpart, controlling the magnetic component of light-matter interactions remains little explored and could add a completely new degree of freedom in photonics and optoelectronics.

Recently, a series of experimental studies have demonstrated the detection[130,132,143-145] and manipulation of magnetic dipole transitions in lanthanide ions by means of metallic and dielectric interfaces in the visible range[56,127,131,146] and by plasmonic cavities in the near infrared[61]. In addition, in the past few years, theoretical studies have predicted the extraordinary properties of a certain class of photonic nanostructures[42], in particular low loss dielectric resonators[8,35,46,52,53,133,147-153] and plasmonic nano-antennas[33,50,51,154], to strongly enhance the optical magnetic field together with the spontaneous emission of magnetic dipoles[8,46,50-53,153,155], making them ideal to open new avenues in the emerging field of magneto-nanophotonics.

In this chapter, I will describe experimentally the ability of photonic nano-antennas to modify either the magnetic or the electric radiative local density of states (LDOS), to manipulate independently the magnetic and electric emission of luminescent emitters in the visible range[156]. I'll show that coupling to a well-designed optical nano-antenna can increase either the magnetic or electric emission of trivalent europium doped nanoparticles, as predicted theoretically[52,153,157]. Finally, placing the antenna at the extremity of an optical scanning tip provides full control over near-field interactions and the ability to record nanoscale maps of

the relative electric and magnetic radiative LDOS (EMLDOS) around resonant nanostructures.

7.1. Manipulating the quantum magnetic emission

Manipulation of the emission of a nanoparticle containing magnetic dipolar (MD) and electric dipolar (ED) transitions in the near field, requires deterministic positioning of a well-defined magnetic or electric antenna in close proximity to the emitter. To this end, and as I described previously in this manuscript, we combined top down focused-ion beam nanostructuring of a thin material (silicon and aluminum) and near-field scanning optical microscopy (NSOM) for control and manipulation at the nanoscale with nanometer precision. Here, two types of nanostructures are chosen: a magnetic cylindrical antenna (MCA) (Figure 7.1a) made of silicon and known to enhance the magnetic field[52,151,153] (Figure 7.1c), and the hybrid nano-antenna referred here as an aluminum electric monopole antenna (EMA) (Figure 7.1b) to enhance the electric field[15,90,158] (Figure 7.1d). As sketched in Figures 7.1a,b, the presence of the optical nano-antenna in close proximity to a crystal containing MD and ED transitions (drawn as a purple particle) modifies the luminescence of the emitter by either enhancing the magnetic (green) or electric (red) emission. Experimentally, we use colloidal nanoparticles (50-70 nm in size) of YVO_4 doped with 20% Eu^{3+}. As shown in the partial band diagram of Figure 7.1e, trivalent europium ions feature MD ($^5D_0$ -> $^7F_1$, 590 nm) and ED ($^5D_0$ -> $^7F_2$, 610 nm) transitions (Figure 7.1f). Their emission spectrum can be therefore tailored by manipulating the EMLDOS with nanostructures. In here, all other decay channels from $^5D_0$ to the ground state are considered as losses.

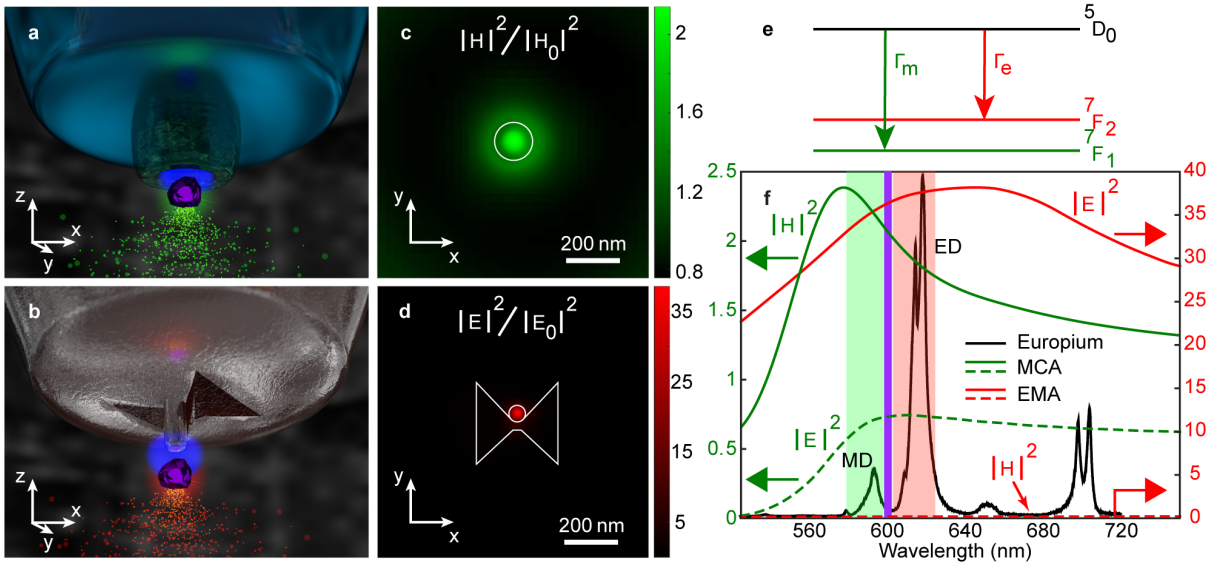

Figure 7.1. *Principle of the experiment. Two types of photonic antennas are carved by a focused-ion beam (FIB) at the extremity of a near field tip. (a) A magnetic cylindrical antenna (MCA) made of silicon and (b) an electric monopole antenna (EMA) made of aluminum are brought in close proximity to a nanocrystal (purple particle) doped with trivalent europium ions featuring both magnetic and electric dipolar transitions. The magnetic emission is denoted in green color and the electric emission in red. (c) and (d) Numerical simulations of the normalized magnetic and electric field intensities in a transversal plane (xy) positioned 10 nm away from the MCA and the EMA respectively (calculated for a 590 nm excitation in the case of the MCA and 610 nm in the case of the EMA), the white circles represent the antennas contours. (e) Partial band diagram of Eu^{3+} describing the magnetic ($^5D_0$ -> $^7F_1$, green) and electric ($^5D_0$ -> $^7F_2$, red) dipolar transitions; Γ_m is the magnetic and Γ_e the electric radiative transition rates. (f) Theoretical magnetic and electric intensity spectral responses, normalized by their respective intensities in vacuum, of the MCA (green continuous and dashed curves) and the EMA (red continuous and dashed curves), calculated 10 nm below the centre of each antenna. The luminescence spectrum of the Eu^{3+} doped nanoparticle is displayed in black. The purple line is the spectral position of the dichroic mirror that splits the magnetic and electric luminescence signals while the green and red bands represent the narrow bandpass filters used for each collection channel.*

Antenna dimensions are set to feature a magnetic dipolar (MCA) and an electric monopolar (EMA) resonance in the visible range (Figure 7.1f), and chosen to differentially cover two different parts of the spectrum so that each antenna mostly affects one transition: the magnetic resonance of the MCA is set to overlap with the MD transition and the electric resonance of the EMA with the ED transition of Eu^{3+} (black curve in Figure 7.1f). Although the resonances appear broad and overlap with both transitions, the magnetic resonance of the MCA will preferentially interact with the magnetic transition of europium and, likewise, for the electric resonance of the EMA.[8] Furthermore, Figure 7.1f provides the spectral evolution of electric and magnetic field intensities simulated 10 nm below the centre of the MCA and the EMA, respectively (dashed curves): both field intensities are actually inhibited with

respect to vacuum (lower than 1) by the nano-antenna and should therefore inhibit electric and magnetic spontaneous emission, respectively, by reciprocity[118].

Figures 7.2a,f display the scanning electron microscope (SEM) images of the MCA and EMA nanofabricated at the end of two different tapered optical fibers. To reveal the ability of both nanostructures to manipulate the emission of the Eu^{3+} doped particle, we performed near field scans of 50-70 nm colloidal europium doped particles, deposited on a glass slide, with both types of antennas. The sample is excited at 465 nm, and the particle luminescence is collected through a high numerical aperture objective, with a dichroic mirror and a set of filters. This leads to the images displayed in Figure 7.2. Figures 7.2b-e correspond to the collected signal when the MCA is scanned over a single nanoparticle, while Figures 7.2g-j show the luminescence measured during the scan of the EMA over a few single particles and a cluster. Figures 7.2b,g depict the total intensity collected, while Figures 7.2c,h and Figures 7.2d,i respectively, provide the signal collected solely in the magnetic (590 nm) and electric (610 nm) channels. Note that these signals arise from the same excited state ($^5D_0$) and therefore are independent of the excitation channel (i.e. in near or far field), which happen at the transition $^7F_0$->$^5D_2$ of Eu^{3+}. As observed, the collected signals corresponding to electric and magnetic emission are significantly modified when coupling a MCA or EMA to the luminescent nanoparticles. In fact, while it is possible to distinguish emission in the case of the MCA in both electric and magnetic channels, in the case of the EMA, the luminescence intensity in the magnetic channel for single particles is negligible. Qualitatively, this can be better appreciated in Figures 7.2e,j where combined pictures are obtained by normalizing the two channels with their respective maxima and by color-coding the magnetic signal in green and the electric one in red. The contrast is striking. In Figure 7.2e, corresponding to the MCA coupled to the particle, both magnetic and electrical signals are detected without spatial overlapping, implying that the maxima of the magnetic and electric radiative LDOS are spatially separated. In contrast, in the particles-EMA case (Figure 7.2j), the signal is clearly dominated by electric spontaneous emission.

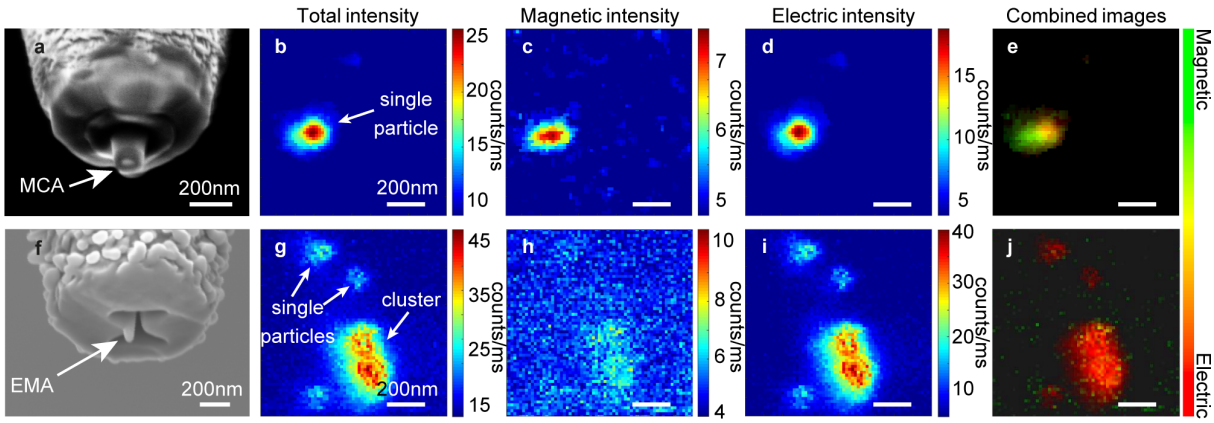

Figure 7.2. *Near field coupling. SEM images of (a), the MCA and (f) the EMA, carved at the extremity of a near-field fiber probe. Luminescence intensity distributions monitored when scanning isolated Eu^{3+} doped nanoparticles in the near-field of a MCA (b-e), or an EMA (g-j): total collected intensity (b,g); collected magnetic emission (c,h); collected electric emission (d,i) and combined images (e,j) obtained by normalizing each detection channel to their maximum and color-coding the magnetic signal in green and the electric counterpart in red, before overlaying.*

To quantitatively retrieve the influence of each nano-antenna on the magneto-electric emission of the nanocrystals, I introduce the branching ratios, which represent the relative weights of the two competing magnetic and electric transitions, and are defined by:[131]

$$\beta_m^{ant} = \frac{\mathrm{I}_m^{lum}}{\mathrm{I}_{total}^{lum}} = \frac{\Gamma_m}{\Gamma_m + \Gamma_e} (2)$$

$$\beta_e^{ant} = 1 - \beta_m^{ant} = \frac{\mathrm{I}_e^{lum}}{\mathrm{I}_{total}^{lum}} = \frac{\Gamma_e}{\Gamma_m + \Gamma_e} (3)$$

where I_m^{lum} and I_e^{lum} stand for the luminescence intensity collected either through the magnetic or electric channel after noise reduction, respectively, and I_{total}^{lum} is the total collected luminescence intensity.

Figures 7.3a,b display the spatial distributions of β_m^{ant} in the case of the MCA (Figure 7.3a) and β_e^{ant} in the case of the EMA (Figure 7.3b), calculated from Figure 7.2. As expected from Figure 7.2, we observe two different trends: in the case of the MCA a clear gradient, going from a dominant magnetic to a dominant electric signal, is seen in the nanoscale variations of β_m^{ant} ; while in the case of the EMA, a constant and essentially electric emission is collected. These trends demonstrate two major effects: first, the EMA is clearly an electric antenna favoring electric emission only. Second, the MCA has a dual property; it can strongly enhance the magnetic emission at given spatial positions, but it can also have an effect on the electric emission when the particle probes other spatial regions of the antenna.

To provide further insight on the nanoscale photonic properties of these resonators, Figures 7.3c and d provide experimental and theoretical line scans of β_m^{ant} and β_e^{ant} for each antenna (inset of Figures 7.3a,b), demonstrating a relatively good agreement. From these line scans, we estimate a 2x average enhancement of the relative signal emanating from the MD transition when introducing the MCA and a 1.3x increase of the relative ED with the EMA with respect to the confocal case (i.e. without antennas).

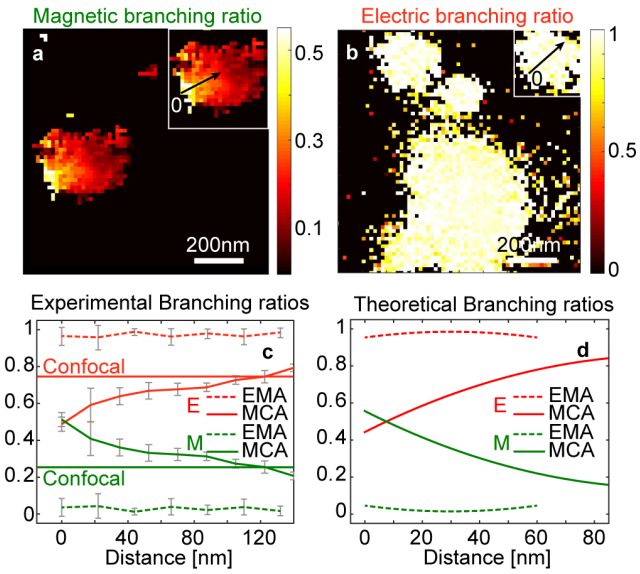

Figure 7.3. *Magnetic and electric branching ratios. (a), Magnetic and (b) electric branching ratio distributions for the MCA and the EMA, respectively. (c) Experimental line scans of the branching ratios represented by the black lines seen in the insets in (a,b); in here, 0 represents the starting point and the arrow the direction of the scan. In (c) green corresponds to the magnetic branching ratio and red, to the electric branching ratios, the confocal constant lines represent the magnetic and electric relative signals detected without the presence of the antennas. The dashed and continuous lines stand for the EMA and MCA, respectively. The error bars represent the standard deviations. (d) Numerical counterpart of (c) where an isotropic MD and ED is scanned over a transverse plane along the MCA and the EMA at a distance of 10 nm below each antenna. The slight discrepancy in distance between experiments and simulations is explained by the fact that numerical simulations consider a single isotropic point source, whereas the luminescent particles have typical dimensions ranging from 50 nm to 70 nm, convoluting the detected signal.*

In addition, it should be mentioned that although the MCA antenna has a cylindrical symmetry, this symmetry is not observed in the branching ratio distributions displayed in Figure 7.3a. This is explained by a shape asymmetry of the fabricated antenna in the longitudinal direction, at final rim of the cylinder, as observed in Figure 7.2a: one side of the antenna is lower than the other inducing this asymmetry in the measured signal, as demonstrated below. As well, a possible tilt of the tip with respect to the sample during the experiment might increase this asymmetry.

7.2. Mapping the electric and magnetic radiative LDOSes

Importantly, since both magnetic and electric transitions are related to the same excited state, the relative weight of each transition given by the branching ratios is directly related to the increase (or decrease) of the radiative magnetic and electric LDOS induced by the antenna:[131]

$$\beta_m^{ant} = \frac{\beta_m^{conf} \cdot \rho_m}{\beta_m^{conf} \cdot \rho_m + \beta_e^{conf} \cdot \rho_e} (4)$$

$$\beta_e^{ant} = 1 - \beta_m^{ant} (5)$$

where β_m^{conf} represents the magnetic and β_e^{conf} the electric branching ratios without the photonic antennas (i.e. far field excitation) (Figure 7.3c), and ρ_m is the magnetic and ρ_e the electric radiative LDOS. Note that here, the strength of each magnetic and electric transition (their relative weight) is estimated to be equal to the branching ratios without the antennas (i.e. β_m^{conf} and β_e^{conf}).

From equations 4 and 5 we therefore introduce the relative radiative magnetic $\tilde{\rho}_m$ and electric $\tilde{\rho}_e$ LDOS[131] as:

$$\tilde{\rho}_m = \frac{\rho_m}{\rho_m + \rho_e} = \frac{\beta_e^{conf} \cdot \beta_m^{ant}}{\beta_e^{conf} \cdot \beta_m^{ant} + \beta_m^{conf} \cdot \beta_e^{ant}} (6)$$

and

$$\tilde{\rho}_e = 1 - \tilde{\rho}_m (7)$$

which represent the relative influence of the antennas on their electric and magnetic quantum environment. Figures 7.4a,b display the spatial distributions of $\tilde{\rho}_m$ and $\tilde{\rho}_e$ around the MCA. Although Figures 7.4a,b seem similar to Figure 7.3a, they actually hold extra information. Indeed, while β_m and β_e describe the relative strengths of two competing transitions, $\tilde{\rho}_m$ and $\tilde{\rho}_e$ quantify the effect of the environment on MD and ED transitions, at a given wavelength and independently of the emitter. Figures 7.4a,b are thus 2D maps of the modification of the electric and magnetic quantum environment surrounding the silicon nanostructured antenna.

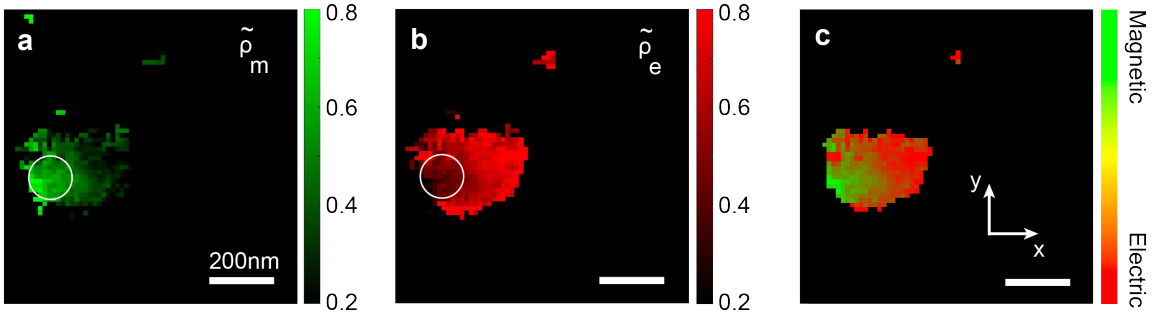

Figure 7.4. *Relative radiative LDOS mapping. (a), magnetic and (b) electric relative radiative LDOS surrounding the MCA, (c) combined LDOS pictures from (a) and (b). The circles represent the outside rim of the MCA.*

Finally, in order to fully express the influence of the antennas on their quantum environment in terms of the relative modification of the magnetic and electric LDOS, we define the degree of magnetic emission (DME) as:

$$\mathrm{DME} = \frac{\tilde{\rho}_m - \tilde{\rho}_e}{\tilde{\rho}_m + \tilde{\rho}_e} \quad (8)$$

Following equation 8, Figures 7.5a,b, display the 2D maps of DME for both antennas. Values of DME lower than 0 describe radiative electric LDOS enhancement (where electric emission is enhanced) and above 0, magnetic LDOS increase (where magnetic emission is increased). As expected, the DME in the case of the EMA is everywhere close to -1 (Figure 7.5b). Interestingly, a large area of about 90x120 nm² features an increase of magnetic emission for the case of the MCA, in good agreement with Figure 7.4f. To be more quantitative, Figures 7.5c,d respectively plot the distribution of DME for each pixel displayed in Figures 7.5a,b, when each antenna is scanning a single particle. We observe a broad distribution in the case of the MCA (Figure 7.5c), with in particular many antenna positions (number of pixels) giving a positive DME, and a very narrow distribution in the case of the EMA (Figure 7.5d), with only negative values and mainly shifted towards -1. These results unambiguously demonstrated an enhancement of magnetic spontaneous emission by means of a photonic nano-antenna (i.e. the MCA).

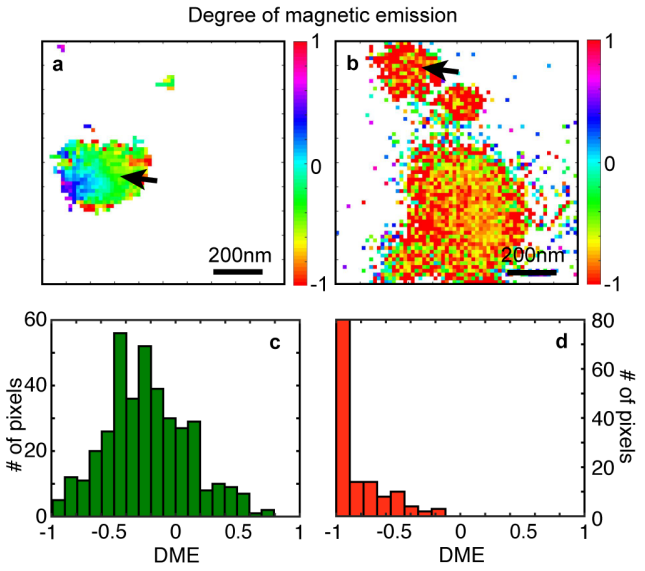

Figure 7.5. *Degree of magnetic emission. DME 2D maps in the case of (a), the MCA and (b) the EMA. (c) and (d) DME distribution obtained over every pixel of respectively (a) and (b) when a single particle is scanned by each antenna (indicated by an arrow), discarding noise pixels.*

In summary, I have shown you, altogether manipulation, enhancement and control of the MD and ED transitions of quantum emitters using photonic nano-antennas, in good agreement

with numerical simulations. Manipulation by allowing the deterministic positioning of a Eu^{3+} doped nanoparticle in close proximity to the nanostructures. Enhancement of respectively 2 and 1.3 times of the relative magnetic and electric emission intensities with respect to far field illumination. Control by designing nanostructures featuring specifically magnetic or electric resonances. Furthermore, I described the spatial distributions of the magnetic and electric relative radiative LDOS surrounding these antennas and the degree of magnetic emission, allowing for a unique insight on how the nanostructures influence their environment at the optical quantum level.

These findings represent a turning point in light-matter interactions, by demonstrating that magnetic spontaneous emission can be dominant over its electric counterpart, thanks to optically resonant nanostructures. In particular, the boost of magnetic light and matter interactions by magnetic nano-antennas opens new paradigms in various research fields involving magnetoelectric couplings such as spintronics, metamaterials, opto-electronics or chiral science. The latter, which is central in modern biochemistry and the evolution of life, would for instance directly benefit from this emerging research, as the magnetic component of light is crucial in light and chiral-matter interactions.[43,159-161]

Papers related to this chapter :

Ernandes, C. *et al.* Exploring the magnetic and electric side of light through plasmonic nanocavities. *Nano Lett.* **18**, 5098-5103 (2018).

Sanz-Paz, M. *et al.* Enhancing magnetic light emission with all-dielectric optical nanoantennas. *Nano. Lett.* **18**, 3481-3487 (2018).

Bidault, S. *et al*. Dielectric nanoantennas to manipulate solid-state light emission. *J. Appl. Phys.* **126**, 094104 (2019).

Bouchet, D. *et al.* Enhancement and inhibition of spontaneous photon emission by resonant silicon nanoantennas. *Physical Review Applied* **6**, 064016 (2016).

General Conclusion

Through this manuscript, I have tried to summarize my scientific career since its origin, namely since my thesis work, and how this journey has defined the directions that my research has taken until today. In particular, after having carried out a thesis that gave me the theoretical and experimental bases for a proper understanding of optical phenomena at the sub-wavelength scale, and in particular the knowledge necessary for the elaboration of optical nanostructures allowing to manipulate the electric and magnetic fields of light separately. After a post-doctoral stay at the ICFO institute in Barcelona, which gave me the keys to master the coupling between optical nano-antennas and single electric quantum emitters. I was able to start developing my own research theme, which aims, as we have seen in the last part of this manuscript, to study and enhance the interactions between "magnetic light" and matter.

Thanks to these different experiences and researches and thanks to the human, technical and financial environment finally at my disposal, I can now tackle new research topics.
In particular, three projects stand out:

The first one concerns the extension of the study of magnetic light and matter interactions. A thesis has just started on this same subject but it will focus on the excitation of magnetic quantum emitters by the optical magnetic field. The idea is to design optical nanoantennas allowing the increase of the optical magnetic field to promote the transfer of energy to matter. Along the same lines, I'd like to demonstrate non-linear optical phenomena generated only by the optical magnetic field. On the magnetic nanoantenna side, we are also currently developing new concepts such as magnetic monopole nanoantennas.

The second project that I am developing in collaboration with Bruno Gallas (CR at the INSP) and on which a PhD student has just started concerns the study of single chiral molecules by non-chiral nanoantennas. Indeed, by exploiting the symmetries of electric and magnetic fields and considering their vectorial part, it is possible to manipulate the interactions between light and chiral molecules without using circular polarizations or chiral nanostructures. In particular, we are interested in organic molecules of living organisms such as light harvesting complexes which are of particular interest.

Finally, the last project on which I wish to work concerns the generation of static magnetic fields in plasmonic nanostructures only by light excitation. Indeed, based on the inverse Faraday effect, which in metals is caused by the emergence of non-linear forces on the free electrons of the metal, it is possible to create continuous currents in the metal. These currents will then create a static magnetic field. By using an advanced nanostructure, designed for example by an evolutionary algorithm, and by applying a high power to it, I believe that it is possible to create magnetic fields of a few teslas at the nanoscale and during very short times, which no technique allows to date. The applications of this type of structures would be extremely numerous; the first of them concerns the writing speed of our hard drive systems. An ANR JCJC will start this year on this subject.

Bibliography

1 Novotny, L. & van Hulst, N. Antennas for light. *Nat. Photonics* **5**, 83-90 (2011).
2 Martin, J. *et al.* High-resolution imaging and spectroscopy of multipolar plasmonic resonances in aluminum nanoantennas. *Nano. Lett.* **14**, 5517-5523 (2014).
3 Singh, A., Calbris, G. & van Hulst, N. F. Vectorial Nanoscale Mapping of Optical Antenna Fields by Single Molecule Dipoles. *Nano. Lett.* **14**, 4715-4723 (2014).
4 Molinaro, C. *et al.* Two-photon luminescence of single colloidal gold nanorods: revealing the origin of plasmon relaxation in small nanocrystals. *J. Phys. Chem. C* **120**, 23136-23143 (2016).
5 Kinkhabwala, A. *et al.* Large single-molecule fluorescence enhancements produced by a bowtie nanoantenna. *Nat. Photonics* **3**, 654-657 (2009).
6 Taminiau, T. H., Moerland, R. J., Segerink, F. B., Kuipers, L. & van Hulst, N. F. λ/4 resonance of an optical monopole antenna probed by single molecule fluorescence. *Nano. Lett.* **7**, 28-33 (2007).
7 Mivelle, M. *et al.* Bowtie nano-aperture as interface between near-fields and a single-mode fiber. *Opt. Express* **18**, 15964-15974 (2010).
8 Rolly, B., Bebey, B., Bidault, S., Stout, B. & Bonod, N. Promoting magnetic dipolar transition in trivalent lanthanide ions with lossless Mie resonances. *Physical Review B* **85**, 245432 (2012).
9 Busson, M. P. *et al.* Optical and topological characterization of gold nanoparticle dimers linked by a single DNA double strand. *Nano. Lett.* **11**, 5060-5065 (2011).
10 Punj, D. *et al.* A plasmonic/antenna-in-box/'platform for enhanced single-molecule analysis at micromolar concentrations. *Nat. Nanotechnol.* (2013).
11 Berthelot, J. *et al.* Three-dimensional manipulation with scanning near-field optical nanotweezers. *Nat. Nanotechnol.* **9**, 295-299 (2014).
12 Lalisse, A. *et al.* Quantitative Temperature Measurements in Gold Nanorods Using Digital Holography. *ACS Applied Materials & Interfaces* (2021).
13 Kruk, S. S. *et al.* Nonlinear optical magnetism revealed by second-harmonic generation in nanoantennas. *Nano. Lett.* **17**, 3914-3918 (2017).
14 Agreda, A. *et al.* Spatial distribution of the nonlinear photoluminescence in au nanowires. *ACS photonics* **6**, 1240-1247 (2019).
15 Taminiau, T., Stefani, F., Segerink, F. & Van Hulst, N. Optical antennas direct single-molecule emission. *Nat. Photonics* **2**, 234-237 (2008).
16 Novotny, L., Pohl, D. & Regli, P. Light propagation through nanometer-sized structures: the two-dimensional-aperture scanning near-field optical microscope. *JOSA A* **11**, 1768-1779 (1994).
17 Mivelle, M. *et al.* Light funneling from a photonic crystal laser cavity to a nano-antenna: overcoming the diffraction limit in optical energy transfer down to the nanoscale. *Opt. Express* **22**, 15075-15087 (2014).
18 Agreda, A. *et al.* Electrostatic Control over Optically Pumped Hot Electrons in Optical Gap Antennas. *ACS photonics* **7**, 2153-2162 (2020).
19 Schuck, P., Fromm, D., Sundaramurthy, A., Kino, G. & Moerner, W. Improving the mismatch between light and nanoscale objects with gold bowtie nanoantennas. *Phys. Rev. Lett.* **94**, 017402 (2005).
20 Wang, L., Uppuluri, S. M., Jin, E. X. & Xu, X. Nanolithography using high transmission nanoscale bowtie apertures. *Nano. Lett.* **6**, 361-364 (2006).
21 Berthelot, J. *et al.* Silencing and enhancement of second-harmonic generation in optical gap antennas. *Opt. Express* **20**, 10498-10508 (2012).

22 Grosjean, T., Mivelle, M., Burr, G. & Baida, F. Optical horn antennas for efficiently transferring photons from a quantum emitter to a single-mode optical fiber. *Opt. Express* **21**, 1762-1772 (2013).
23 Ibrahim, I. A. *et al.* Bowtie-shaped nanoaperture: a modal study. *Opt. Lett.* **35**, 2448-2450 (2010).
24 Bachelot, R., Ecoffet, C., Deloeil, D., Royer, P. & Lougnot, D.-J. Integration of micrometer-sized polymer elements at the end of optical fibers by free-radical photopolymerization. *Appl. Opt.* **40**, 5860-5871 (2001).
25 Martin, J. & Plain, J. Fabrication of aluminium nanostructures for plasmonics. *J. Phys. D: Appl. Phys.* **48**, 184002 (2014).
26 Grober, R. D., Schoelkopf, R. J. & Prober, D. E. Optical antenna: Towards a unity efficiency near-field optical probe. *Appl. Phys. Lett.* **70**, 1354-1356 (1997).
27 Guo, R. *et al.* Three-dimensional mapping of optical near field of a nanoscale bowtie antenna. (2010).
28 Le Gac, G. *et al.* Tuning of an active photonic crystal cavity by an hybrid silica/silicon near-field probe. *Opt. Express* **17**, 21672-21679 (2009).
29 van Zanten, T. S. *et al.* Direct mapping of nanoscale compositional connectivity on intact cell membranes. *Proceedings of the National Academy of Sciences* **107**, 15437-15442 (2010).
30 Suarez, M., Grosjean, T., Charraut, D. & Courjon, D. Nanoring as a magnetic or electric field sensitive nano-antenna for near-field optics applications. *Opt. Commun.* **270**, 447-454 (2007).
31 Zhou, J. *et al.* Saturation of the magnetic response of split-ring resonators at optical frequencies. *Phys. Rev. Lett.* **95**, 223902 (2005).
32 Zentgraf, T. *et al.* Babinet's principle for optical frequency metamaterials and nanoantennas. *Phys. Rev. B* **76**, 033407 (2007).
33 Grosjean, T., Mivelle, M., Baida, F., Burr, G. & Fischer, U. Diabolo nanoantenna for enhancing and confining the magnetic optical field. *Nano. Lett.* **11**, 1009-1013 (2011).
34 Zhou, N., Kinzel, E. C. & Xu, X. Complementary bowtie aperture for localizing and enhancing optical magnetic field. *Opt. Lett.* **36**, 2764-2766 (2011).
35 Evlyukhin, A. B. *et al.* Demonstration of magnetic dipole resonances of dielectric nanospheres in the visible region. *Nano Lett.* **12**, 3749-3755 (2012).
36 Ginn, J. C. *et al.* Realizing optical magnetism from dielectric metamaterials. *Phys. Rev. Lett.* **108**, 097402 (2012).
37 Boudarham, G., Abdeddaim, R. & Bonod, N. Enhancing the magnetic field intensity with a dielectric gap antenna. *Appl. Phys. Lett.* **104**, 021117 (2014).
38 Landau, L. D., Lífshíts, E. M. & Pitaevskii, L. *Electrodynamics of continuous media*. Vol. 8 (Pergamon press Oxford, 1984).
39 Cowan, R. D. *The theory of atomic structure and spectra*. Vol. 3 (Univ of California Press, 1981).
40 Burresi, M. *et al.* Probing the magnetic field of light at optical frequencies. *Science* **326**, 550-553 (2009).
41 Giessen, H. & Vogelgesang, R. Glimpsing the weak magnetic field of light. *Science* **326**, 529-530 (2009).
42 Baranov, D. G., Savelev, R. S., Li, S. V., Krasnok, A. E. & Alù, A. Modifying magnetic dipole spontaneous emission with nanophotonic structures. *Laser & Photonics Reviews* **11**, 1600268 (2017).
43 Valev, V. K., Govorov, A. O. & Pendry, J. Chirality and Nanophotonics. *Advanced Optical Materials* **5** (2017).

44 Xi, Z. & Urbach, H. Magnetic Dipole Scattering from Metallic Nanowire for Ultrasensitive Deflection Sensing. *Phys. Rev. Lett.* **119**, 053902 (2017).
45 Manjavacas, A. *et al.* Magnetic light and forbidden photochemistry: the case of singlet oxygen. *Journal of Materials Chemistry C* **5**, 11824-11831 (2017).
46 Albella, P. *et al.* Low-loss Electric and Magnetic Field-Enhanced Spectroscopy with subwavelength silicon dimers. *J. Phys. Chem. C* **117**, 13573-13584 (2013).
47 Blanco, M. *et al.* Ultraintense femtosecond magnetic nanoprobes induced by azimuthally polarized laser beams. *ACS Photonics* **6**, 38-42 (2018).
48 Calandrini, E., Cerea, A., De Angelis, F., Zaccaria, R. P. & Toma, A. Magnetic hot-spot generation at optical frequencies: from plasmonic metamolecules to all-dielectric nanoclusters. *Nanophotonics* **8**, 45-62 (2018).
49 Feng, T., Zhou, Y., Liu, D. & Li, J. Controlling magnetic dipole transition with magnetic plasmonic structures. *Opt. Lett.* **36**, 2369-2371 (2011).
50 Hein, S. M. & Giessen, H. Tailoring Magnetic Dipole Emission with Plasmonic Split-Ring Resonators. *Phys. Rev. Lett.* **111**, 026803 (2013).
51 Mivelle, M., Grosjean, T., Burr, G. W., Fischer, U. C. & Garcia-Parajo, M. F. Strong Modification of Magnetic Dipole Emission through Diabolo Nanoantennas. *ACS Photonics* **2**, 1071-1076 (2015).
52 Feng, T., Xu, Y., Liang, Z. & Zhang, W. All-dielectric hollow nanodisk for tailoring magnetic dipole emission. *Optics Letters* **41**, 5011-5014 (2016).
53 Kuznetsov, A. I., Miroshnichenko, A. E., Brongersma, M. L., Kivshar, Y. S. & Luk'yanchuk, B. Optically resonant dielectric nanostructures. *Science* **354**, aag2472 (2016).
54 Feng, T., Zhang, W., Liang, Z., Xu, Y. & Miroshnichenko, A. E. Isotropic magnetic Purcell effect. *ACS Photonics* **5**, 678-683 (2017).
55 Li, J., Verellen, N. & Van Dorpe, P. Enhancing Magnetic Dipole Emission by a Nano-Doughnut-Shaped Silicon Disk. *ACS Photonics* **4**, 1893-1898 (2017).
56 Hussain, R. *et al.* Enhancing Eu 3+ magnetic dipole emission by resonant plasmonic nanostructures. *Opt. Lett.* **40**, 1659-1662 (2015).
57 Ernandes, C. *et al.* Exploring the magnetic and electric side of light through plasmonic nanocavities. *Nano Lett.* **18**, 5098-5103 (2018).
58 Sanz-Paz, M. *et al.* Enhancing magnetic light emission with all-dielectric optical nanoantennas. *Nano Lett.* **18**, 3481-3487 (2018).
59 Wiecha, P. R. *et al.* Simultaneous mapping of the electric and magnetic photonic local density of states above dielectric nanostructures using rare-earth doped films. *arXiv preprint arXiv:1801.09690* (2018).
60 Vaskin, A. *et al.* Manipulation of magnetic dipole emission from Eu3+ with Mie-resonant dielectric metasurfaces. *Nano Lett.* (2019).
61 Choi, B., Iwanaga, M., Sugimoto, Y., Sakoda, K. & Miyazaki, H. T. Selective Plasmonic Enhancement of Electric-and Magnetic-Dipole Radiations of Er Ions. *Nano Lett.* **16**, 5191-5196 (2016).
62 Kuznetsov, A. I., Miroshnichenko, A. E., Fu, Y. H., Zhang, J. & Luk'Yanchuk, B. Magnetic light. *Scientific reports* **2**, 492 (2012).
63 Molesky, S. *et al.* Inverse design in nanophotonics. *Nat. Photonics* **12**, 659 (2018).
64 Feichtner, T., Selig, O., Kiunke, M. & Hecht, B. Evolutionary optimization of optical antennas. *Phys. Rev. Lett.* **109**, 127701 (2012).
65 Feichtner, T., Selig, O. & Hecht, B. Plasmonic nanoantenna design and fabrication based on evolutionary optimization. *Opt. Express* **25**, 10828-10842 (2017).
66 Wiecha, P. R. *et al.* Evolutionary multi-objective optimization of colour pixels based on dielectric nanoantennas. *Nat. Nanotechnol.* **12**, 163 (2017).

67 Piggott, A. Y. *et al.* Inverse design and demonstration of a compact and broadband on-chip wavelength demultiplexer. *Nat. Photonics* **9**, 374-377 (2015).
68 Su, L., Piggott, A. Y., Sapra, N. V., Petykiewicz, J. & Vuckovic, J. Inverse design and demonstration of a compact on-chip narrowband three-channel wavelength demultiplexer. *ACS Photonics* **5**, 301-305 (2017).
69 Yu, Z., Cui, H. & Sun, X. Genetically optimized on-chip wideband ultracompact reflectors and Fabry–Perot cavities. *Photonics Research* **5**, B15-B19 (2017).
70 Asano, T. & Noda, S. Optimization of photonic crystal nanocavities based on deep learning. *Opt. Express* **26**, 32704-32717 (2018).
71 Jin, Z. *et al.* Complex Inverse Design of Meta-optics by Segmented Hierarchical Evolutionary Algorithm. *ACS Nano* (2019).
72 Bonod, N., Bidault, S., Burr, G. W. & Mivelle, M. Evolutionary Optimization of All−Dielectric Magnetic Nanoantennas. *Advanced Optical Materials* **7**, 1900121 (2019).
73 Li, D. *et al.* Quantifying and controlling the magnetic dipole contribution to 1.5− μ m light emission in erbium-doped yttrium oxide. *Phys. Rev. B* **89**, 161409 (2014).
74 Hell, S. W. Far-field optical nanoscopy. *science* **316**, 1153-1158 (2007).
75 Huang, B., Babcock, H. & Zhuang, X. Breaking the diffraction barrier: super-resolution imaging of cells. *Cell* **143**, 1047-1058 (2010).
76 Kanchanawong, P. *et al.* Nanoscale architecture of integrin-based cell adhesions. *Nature* **468**, 580-584 (2010).
77 Schermelleh, L., Heintzmann, R. & Leonhardt, H. A guide to super-resolution fluorescence microscopy. *The Journal of cell biology* **190**, 165-175 (2010).
78 Xu, K., Zhong, G. & Zhuang, X. Actin, spectrin, and associated proteins form a periodic cytoskeletal structure in axons. *Science* **339**, 452-456 (2013).
79 Klar, T. A., Jakobs, S., Dyba, M., Egner, A. & Hell, S. W. Fluorescence microscopy with diffraction resolution barrier broken by stimulated emission. *Proceedings of the National Academy of Sciences* **97**, 8206-8210 (2000).
80 Betzig, E. *et al.* Imaging intracellular fluorescent proteins at nanometer resolution. *Science* **313**, 1642-1645 (2006).
81 Hess, S. T., Girirajan, T. P. & Mason, M. D. Ultra-high resolution imaging by fluorescence photoactivation localization microscopy. *Biophys. J.* **91**, 4258-4272 (2006).
82 Rust, M. J., Bates, M. & Zhuang, X. Sub-diffraction-limit imaging by stochastic optical reconstruction microscopy (STORM). *Nat. Methods* **3**, 793-796 (2006).
83 Rittweger, E., Han, K. Y., Irvine, S. E., Eggeling, C. & Hell, S. W. STED microscopy reveals crystal colour centres with nanometric resolution. *Nat. Photonics* **3**, 144-147 (2009).
84 Pertsinidis, A. *et al.* Ultrahigh-resolution imaging reveals formation of neuronal SNARE/Munc18 complexes in situ. *Proceedings of the National Academy of Sciences* **110**, E2812-E2820 (2013).
85 Betzig, E. & Chichester, R. J. Single molecules observed by near-field scanning optical microscopy. *Science* **262**, 1422-1425 (1993).
86 Garcia-Parajo, M. F. Optical antennas focus in on biology. *Nat. Photonics* **2**, 201-203 (2008).
87 Mühlschlegel, P., Eisler, H.-J., Martin, O., Hecht, B. & Pohl, D. Resonant optical antennas. *Science* **308**, 1607-1609 (2005).
88 El Harfouch, Y. *et al.* in *Nanophotonics Iv.* 842418 (International Society for Optics and Photonics).
89 van Zanten, T. S., Lopez−Bosque, M. J. & Garcia−Parajo, M. F. Imaging Individual Proteins and Nanodomains on Intact Cell Membranes with a Probe−Based Optical Antenna. *Small* **6**, 270-275 (2010).

90 Mivelle, M., van Zanten, T. S. & Garcia-Parajo, M. F. Hybrid photonic antennas for subnanometer multicolor localization and nanoimaging of single molecules. *Nano. Lett.* **14**, 4895-4900 (2014).
91 Mivelle, M., van Zanten, T. S., Neumann, L., van Hulst, N. F. & Garcia-Parajo, M. F. Ultrabright Bowtie Nanoaperture Antenna Probes Studied by Single Molecule Fluorescence. *Nano. Lett.* **12**, 5972-5978 (2012).
92 Taminiau, T., Stefani, F. & Van Hulst, N. Single emitters coupled to plasmonic nano-antennas: angular emission and collection efficiency. *New Journal of Physics* **10**, 105005 (2008).
93 Moerland, R. J., Taminiau, T. H., Novotny, L., Van Hulst, N. F. & Kuipers, L. Reversible polarization control of single photon emission. *Nano. Lett.* **8**, 606-610 (2008).
94 Pertsinidis, A., Zhang, Y. & Chu, S. Subnanometre single-molecule localization, registration and distance measurements. *Nature* **466**, 647-651 (2010).
95 Manzo, C., van Zanten, T. S. & Garcia-Parajo, M. F. Nanoscale fluorescence correlation spectroscopy on intact living cell membranes with NSOM probes. *Biophys. J.* **100**, L8-L10 (2011).
96 Winkler, P. M., Regmi, R. & Flauraud, V. Vol. 9 110 (2018).
97 Wenger, J. *et al.* Emission and excitation contributions to enhanced single molecule fluorescence by gold nanometric apertures. *Opt. Express* **16**, 3008-3020 (2008).
98 Anger, P., Bharadwaj, P. & Novotny, L. Enhancement and quenching of single-molecule fluorescence. *Phys. Rev. Lett.* **96**, 113002 (2006).
99 Bharadwaj, P., Anger, P. & Novotny, L. Nanoplasmonic enhancement of single-molecule fluorescence. *Nanotechnology* **18**, 044017 (2006).
100 Flauraud, V. *et al.* In-plane plasmonic antenna arrays with surface nanogaps for giant fluorescence enhancement. *Nano. Lett.* **17**, 1703-1710 (2017).
101 Andrew, P. & Barnes, W. L. Förster energy transfer in an optical microcavity. *Science* **290**, 785-788 (2000).
102 Truong, K. & Ikura, M. The use of FRET imaging microscopy to detect protein–protein interactions and protein conformational changes in vivo. *Curr. Opin. Struct. Biol.* **11**, 573-578 (2001).
103 Clegg, R. Curr. Opin. Biotechnol. *Curr. Opin. Biotechnol.* **6**, 103-110 (1995).
104 De Torres, J. *et al.* Plasmonic Nanoantennas Enable Forbidden Förster Dipole–Dipole Energy Transfer and Enhance the FRET Efficiency. *Nano. Lett.* **16**, 6222-6230 (2016).
105 Ghenuche, P. *et al.* Matching Nanoantenna Field Confinement to FRET Distances Enhances Förster Energy Transfer Rates. *Nano. Lett.* **15**, 6193-6201 (2015).
106 Aissaoui, N. *et al.* FRET enhancement close to gold nanoparticles positioned in DNA origami constructs. *Nanoscale* **9**, 673-683 (2017).
107 Blum, C. *et al.* Nanophotonic control of the Förster resonance energy transfer efficiency. *Phys. Rev. Lett.* **109**, 203601 (2012).
108 Konrad, A., Metzger, M., Kern, A. M., Brecht, M. & Meixner, A. J. Controlling the dynamics of Förster resonance energy transfer inside a tunable sub-wavelength Fabry–Pérot-resonator. *Nanoscale* **7**, 10204-10209 (2015).
109 Zurita-Sánchez, J. R. & Méndez-Villanueva, J. Förster energy transfer in the vicinity of two metallic nanospheres (dimer). *Plasmonics* **13**, 873-883 (2018).
110 Rustomji, K. *et al.* Direct imaging of the energy-transfer enhancement between two dipoles in a photonic cavity. *Physical Review X* **9**, 011041 (2019).
111 Zhang, J., Fu, Y. & Lakowicz, J. R. Enhanced Förster resonance energy transfer (FRET) on a single metal particle. *J. Phys. Chem. C* **111**, 50-56 (2007).

112 Baibakov, M. *et al.* Extending Single-Molecule Förster Resonance Energy Transfer (FRET) Range beyond 10 Nanometers in Zero-Mode Waveguides. *ACS Nano* **13**, 8469-8480 (2019).
113 Schreiber, B. *et al.* Enhanced fluorescence resonance energy transfer in G-protein-coupled receptor probes on nanocoated microscopy coverslips. *ACS Photonics* **5**, 2225-2233 (2018).
114 Zhao, T., Li, T. & Liu, Y. Silver nanoparticle plasmonic enhanced förster resonance energy transfer (FRET) imaging of protein-specific sialylation on the cell surface. *Nanoscale* **9**, 9841-9847 (2017).
115 Curto, A. G. *et al.* Unidirectional emission of a quantum dot coupled to a nanoantenna. *Science* **329**, 930-933 (2010).
116 Yao, K. & Liu, Y. Controlling electric and magnetic resonances for ultracompact nanoantennas with tunable directionality. *ACS Photonics* **3**, 953-963 (2016).
117 Hübner, K. *et al.* Directing single-molecule emission with DNA origami-assembled optical antennas. *Nano. Lett.* **19**, 6629-6634 (2019).
118 Novotny, L. & Hecht, B. *Principles of nano-optics*. (Cambridge university press, 2012).
119 Bohlen, J. *et al.* Plasmon-assisted Förster resonance energy transfer at the single-molecule level in the moderate quenching regime. *Nanoscale* **11**, 7674-7681 (2019).
120 Bidault, S. *et al.* Competition between Forster resonance energy transfer and donor photodynamics in plasmonic dimer nanoantennas. *ACS photonics* **3**, 895-903 (2016).
121 Cortes, C. L. & Jacob, Z. Fundamental figures of merit for engineering Förster resonance energy transfer. *Opt. Express* **26**, 19371-19387 (2018).
122 Vahala, K. J. Optical microcavities. *Nature* **424**, 839-846 (2003).
123 Lodahl, P. *et al.* Controlling the dynamics of spontaneous emission from quantum dots by photonic crystals. *Nature* **430**, 654-657 (2004).
124 Kühn, S., Håkanson, U., Rogobete, L. & Sandoghdar, V. Enhancement of single-molecule fluorescence using a gold nanoparticle as an optical nanoantenna. *Physical review letters* **97**, 017402 (2006).
125 Purcell, E. M. Spontaneous emission probabilities at radio frequencies. *Phys. Rev.* **69**, 681 (1946).
126 Grynberg, G., Aspect, A. & Fabre, C. Introduction to quantum optics: from the semi-classical approach to quantized light. (Cambridge university press, 2010).
127 Noginova, N., Barnakov, Y., Li, H. & Noginov, M. Effect of metallic surface on electric dipole and magnetic dipole emission transitions in Eu< sup> 3+</sup> doped polymeric film. *Optics express* **17**, 10767-10772 (2009).
128 Karaveli, S. & Zia, R. Strong enhancement of magnetic dipole emission in a multilevel electronic system. *Opt. Lett.* **35**, 3318-3320 (2010).
129 Karaveli, S., Wang, S., Xiao, G. & Zia, R. Time-Resolved Energy-Momentum Spectroscopy of Electric and Magnetic Dipole Transitions in Cr3+: MgO. *ACS Nano* **7**, 7165-7172 (2013).
130 Taminiau, T. H., Karaveli, S., van Hulst, N. F. & Zia, R. Quantifying the magnetic nature of light emission. *Nature communications* **3**, 979 (2012).
131 Aigouy, L., Cazé, A., Gredin, P., Mortier, M. & Carminati, R. Mapping and quantifying electric and magnetic dipole luminescence at the nanoscale. *Phys. Rev. Lett.* **113**, 076101 (2014).
132 Karaveli, S. & Zia, R. Spectral tuning by selective enhancement of electric and magnetic dipole emission. *Physical review letters* **106**, 193004 (2011).
133 García-Etxarri, A. *et al.* Strong magnetic response of submicron silicon particles in the infrared. *Opt. Express* **19**, 4815-4826 (2011).

134 Pakizeh, T., Abrishamian, M., Granpayeh, N., Dmitriev, A. & Käll, M. Magnetic-field enhancement in gold nanosandwiches. *Opt. Express* **14**, 8240-8246 (2006).
135 Pakizeh, T., Dmitriev, A., Abrishamian, M., Granpayeh, N. & Käll, M. Structural asymmetry and induced optical magnetism in plasmonic nanosandwiches. *JOSA B* **25**, 659-667 (2008).
136 Kaminski, F., Sandoghdar, V. & Agio, M. Finite-difference time-domain modeling of decay rates in the near field of metal nanostructures. *J. Comput. Theor. Nanosci.* **4**, 635-643 (2007).
137 Chance, R., Prock, A. & Silbey, R. Molecular fluorescence and energy transfer near interfaces. *Adv. Chem. Phys* **37**, 65 (1978).
138 Caldarola, M. *et al.* Non-plasmonic nanoantennas for surface enhanced spectroscopies with ultra-low heat conversion. *Nat. Commun.* **6**, 7915 (2015).
139 Staude, I. *et al.* Shaping photoluminescence spectra with magnetoelectric resonances in all-dielectric nanoparticles. *ACS Photonics* **2**, 172-177 (2015).
140 Bouchet, D. *et al.* Enhancement and inhibition of spontaneous photon emission by resonant silicon nanoantennas. *Physical Review Applied* **6**, 064016 (2016).
141 Regmi, R. *et al.* All-Dielectric Silicon Nanogap Antennas To Enhance the Fluorescence of Single Molecules. *Nano Letters* **16**, 5143-5151 (2016).
142 Bidault, S., Mivelle, M. & Bonod, N. Dielectric nanoantennas to manipulate solid-state light emission. *J. Appl. Phys.* **126**, 094104 (2019).
143 Karaveli, S., Weinstein, A. J. & Zia, R. Direct modulation of lanthanide emission at sub-lifetime scales. *Nano Lett.* **13**, 2264-2269 (2013).
144 Cueff, S. *et al.* Dynamic control of light emission faster than the lifetime limit using VO 2 phase-change. *Nat. Commun.* **6**, 8636 (2015).
145 Kasperczyk, M., Person, S., Ananias, D., Carlos, L. D. & Novotny, L. Excitation of magnetic dipole transitions at optical frequencies. *Physical review letters* **114**, 163903 (2015).
146 Rabouw, F. T., Prins, P. T. & Norris, D. J. Europium-Doped NaYF4 Nanocrystals as Probes for the Electric and Magnetic Local Density of Optical States throughout the Visible Spectral Range. *Nano Letters* **16**, 7254-7260 (2016).
147 Evlyukhin, A. B., Reinhardt, C., Seidel, A., Luk'yanchuk, B. S. & Chichkov, B. N. Optical response features of Si-nanoparticle arrays. *Phys. Rev. B* **82**, 045404 (2010).
148 Schmidt, M. K. *et al.* Dielectric antennas-a suitable platform for controlling magnetic dipolar emission. *Opt. Express* **20**, 13636-13650 (2012).
149 Coenen, T., Van De Groep, J. & Polman, A. Resonant modes of single silicon nanocavities excited by electron irradiation. *ACS Nano* **7**, 1689-1698 (2013).
150 Zambrana-Puyalto, X. & Bonod, N. Purcell factor of spherical Mie resonators. *Phys. Rev. B* **91**, 195422 (2015).
151 van de Haar, M. A., van de Groep, J., Brenny, B. J. & Polman, A. Controlling magnetic and electric dipole modes in hollow silicon nanocylinders. *Optics express* **24**, 2047-2064 (2016).
152 Cihan, A. F., Curto, A. G., Raza, S., Kik, P. G. & Brongersma, M. L. Silicon Mie Resonators for Highly Directional Light Emission from monolayer MoS2. *arXiv preprint arXiv:1709.04999* (2017).
153 Li, J., Verellen, N. & Van Dorpe, P. Enhancing Magnetic Dipole Emission by a Nano-Doughnut-Shaped Silicon Disk. *ACS Photonics* (2017).
154 Chigrin, D. N., Kumar, D., Cuma, D. & von Plessen, G. Emission Quenching of Magnetic Dipole Transitions near a Metal Nanoparticle. *ACS Photonics* **3**, 27-34 (2015).

155 Baranov, D. G., Savelev, R. S., Li, S. V., Krasnok, A. E. & Alù, A. Modifying magnetic dipole spontaneous emission with nanophotonic structures. *Laser & Photonics Reviews* (2017).
156 Sanz-Paz, M. *et al.* Enhancing Magnetic Light Emission with All-Dielectric Optical Nanoantennas. *Nano. Lett.* **18**, 3481-3487 (2018).
157 Feng, T., Zhang, W., Liang, Z., Xu, Y. & Miroshnichenko, A. E. Isotropic Magnetic Purcell Effect. *ACS Photonics* (2017).
158 Sanz-Paz, M., Wenger, J., van Hulst, N. F., Mivelle, M. & Garcia-Parajo, M. F. Nanoscale control of single molecule Förster resonance energy transfer by a scanning photonic nanoantenna. *Nanophotonics* **1** (2020).
159 Tang, Y. & Cohen, A. E. Optical chirality and its interaction with matter. *Phys. Rev. Lett.* **104**, 163901 (2010).
160 Klimov, V. V., Guzatov, D. V. & Ducloy, M. Engineering of radiation of optically active molecules with chiral nano-meta-particles. *EPL (Europhysics Letters)* **97**, 47004 (2012).
161 Ho, C.-S., Garcia-Etxarri, A., Zhao, Y. & Dionne, J. Enhancing enantioselective absorption using dielectric nanospheres. *ACS Photonics* **4**, 197-203 (2017).